RECONSTRUCTION OF HIGH ARCTIC WINTER SURFACE ENERGY FLUXES

by

Colin Pike-Thackray

Submitted in partial fulfillment of the requirements
for the degree of Master of Science

at

Dalhousie University
Halifax, Nova Scotia
August 2011

DALHOUSIE UNIVERSITY

DEPARTMENT OF PHYSICS AND ATMOSPHERIC SCIENCE

The undersigned hereby certify that they have read and recommend to the Faculty of Graduate Studies for acceptance a thesis entitled "RECONSTRUCTION OF HIGH ARCTIC WINTER SURFACE ENERGY FLUXES" by Colin Pike-Thackray in partial fulfillment of the requirements for the degree of Master of Science.

Dated: August 5, 2011

Supervisor: _____

Readers: _____

_____

DALHOUSIE UNIVERSITY

DATE: August 5, 2011

AUTHOR: Colin Pike-Thackray

TITLE: RECONSTRUCTION OF HIGH ARCTIC WINTER SURFACE ENERGY FLUXES

DEPARTMENT OR SCHOOL: Department of Physics and Atmospheric Science

DEGREE: M.Sc. CONVOCATION: October YEAR: 2011

Signature of Author

TABLE OF CONTENTS

LIST OF TABLES

LIST OF FIGURES

ABSTRACT

Throughout the late 20^{th} and early 21^{st} century, the global temperature has been on the rise, a process that has been accelerated in the Arctic. The Arctic surface temperatures have risen at a factor of 3 greater rate than the global average, leading to the term Arctic Amplification of climate change.

In this study, the enhanced warming of the Arctic, and the enhancement at the Arctic surface in comparison to the warming of the atmosphere aloft, is investigated through a reconstruction of the past surface energy balance by a model driven by downwelling irradiance reconstructed using radiosonde profiles and the radiative transfer code SBDART. The downwelling irradiance is shown to be increasing over the time-period of 1994-2009, and the sources of this increase are diagnosed. The time-evolution of the surface flux terms are discussed, and the sensitivity of the surface temperature to changes in atmospheric temperature is investigated.

LIST OF ABBREVIATIONS AND SYMBOLS USED

Symbol	Description	Units
DW	downwelling long-wave irradiance	Wm^{-2}
UW	upwelling long-wave irradiance	Wm^{-2}
SH	sensible heat flux to surface	Wm^{-2}
LH	latent heat flux to surface	Wm^{-2}
C	conductive flux to surface	Wm^{-2}
T_s	surface skin temperature	K
k_{snow}	thermal conductivity of snow	$\mathrm{Wm}^{-1}\mathrm{K}^{-1}$
k_{soil}	thermal conductivity of soil	$\mathrm{Wm}^{-1}\mathrm{K}^{-1}$
u	wind speed	m/s
C_s	bulk transfer coefficient of sensible heat	none
C_e	bulk transfer coefficient of latent heat	none
θ	potential temperature	K
q	water vapour mixing ratio	g/kg
ϵ	emissivity	none
A_s	surface amplification factor	none

ACKNOWLEDGEMENTS

First of all, thanks goes to Tom Duck for his supervision over the two years of my Master's degree and for the opportunities that he has given me as a member of his group. By definition, this thesis could not have been written without him. An equally important thank you goes to Glen Lesins for his guidance over the course of my time at Dalhousie, and particularly for his invaluable help and steady supply of knowledge as the thesis developed.

Another pair of people who helped make this work possible are Kaz Higuchi and Shannon Allen at Environment Canada, who granted me access to, and supplied help with, the data archive that was used in this work. Thanks is also given to Nobuki Matsui and NOAA for the dicussion and use of their measurements. I am thankful for the input and discussion of the AOLab group: Chris Perro, Graeme Nott, Jon Doyle, Jason Hopper (and Emily McCullough).

For increasing the degree of difficulty of writing while on campus, I'd like to thank Ryan Robski and Chris Perro, and their daily desire to play cards.

I would finally like to thank Jeff Pierce and Jonathan Franklin for their constant willingness to talk science, be it about my work, their work, or anything else interesting that might come up.

CHAPTER 1

INTRODUCTION

The planet Earth has been warming significantly since the industrial revolution, when we (as humans) started proficiently putting extra greenhouse gases in the atmosphere. While this long-term trend is troubling, more worrisome is the enhanced effect that global warming is having at the poles. The Arctic, for instance, has been warming at a rate of 0.58 K per decade, and 0.88 K per decade at Eureka (80° N, 85° W) in particular (*Lesins et al.*, 2010), over the last 30 years, whereas the global average warming has only been 0.2 K/decade (*Chylek et al.*, 2009). This factor of 3 difference has led to the term Arctic Amplification (*Serreze and Francis*, 2006) when talking about climate change. While causes for warming in general are well-documented, the cause of this warming enhancement in the Arctic is still uncertain.

Previous studies have suggested that sea ice loss (*Manabe and Stouffer*, 1980),(*Hansen et al.*, 2005),(*Screen and Simmons*, 2010) creates an increase in sensible heat flux from the less insulated oceans, and lessens the amount of sea-ice present at the end of summer. This, in turn, allows the ocean to absorb more solar energy due to the lower albedo and delay the insulation of the cooling atmosphere from the warmer ocean (*Serreze et al.*, 2009). The same conclusions are drawn from climate models, as polar amplification is prevalent in model predictions with thinner sea-ice (*Holland and Bitz*, 2003).

Changes in ocean circulation have also been suggested as causes for amplification of warming in the Arctic (*Moritz et al.*, 2002),(*Alexeev et al.*, 2005), as well as changes in the important greenhouse gases such as water vapour (*Francis and Hunter*, 2007). Another suggested factor in Arctic Amplification is the transport of heat from the lower latitudes to

the north (*Graversen*, 2006). It is proposed that increased northward energy transfer occurs linked to baroclinic weather systems developing around the Icelandic and Aleutian lows.

During the winter, an important feature of the Arctic environment is the persistent temperature inversion at the surface. This inversion can be stronger than 30 K over less than 1 km altitude, and can be present for days to weeks (*Bradley and Keimig*, 1992). This extreme stability effectively decouples the surface from the air aloft, and greatly hinders the exchange of energy between the lower and upper troposphere. The Arctic surface is then most susceptible to changes in radiative forcing and to energy transfered from the ocean or soil below. The focus of many of the above Arctic studies is warming above the sea ice, whereas there is less discussion of the warming that happens specifically over the Arctic Archipelago.

The purpose of this work is to provide a starting point and a proof of concept for the understanding of enhanced Arctic warming during winter in the context of surface energy balance at two land sites: Eureka and Resolute. These sites are both Environment Canada (EC) weather stations in the Nunavut Territory. They were chosen for a few reasons, the first being that they are in the High Arctic. Resolute is at 74° N and Eureka is even higher at 80° N, meaning that they each get a sun-less winter. The second reason is that they are EC weather stations, and so are the location of launches of critical radiosonde balloons every 12 hours. The final reason is that they each have something unique to provide to this study; for Eureka it is the presence of multiple lidars to aid and assess the modeling of atmospheric radiation (*not* their only use), and for Resolute it is the soil temperature measurements which took place for over 20 years in the 60's, 70's and 80's but were unfortunately discontinued.

The surface energy budget includes various terms, in the form of radiation, conduction, and turbulence. Although all are flows of energy, their mechanisms are very different, and to predict or diagnose them all takes a variety of methods. Chapter 2 will be a discussion of the atmospheric radiation which drives the surface balance from above. The downwelling radiative flux, specifically in the form of infrared radiation, is the largest supplier to the energy budget. It is therefore important to properly characterize it, which is the purpose of Chapter 2. A method is introduced to diagnose historical winter atmospheric radiation using a radiative transfer code and balloon soundings of the atmosphere which occur every twelve hours at our chosen locations of study. Along the way, a method for the prediction

of cloud layers is used in this endeavor, as clouds are an important source of atmospheric long-wave radiation. This method is compared to direct and indirect measurements as an assessment.

With the radiation term in hand, the focus of the next chapter (Chapter 3) becomes the conductive flux from below the surface. Since conductive heat flows down the temperature gradient, this is effectively a source of energy to the surface during the winter, as the soil remains warmer than the surface above it until after the sun comes out in the spring. For the study of surface balance, a conduction model is introduced which will provide the temperature behaviour below the surface, allowing a diagnosis of the conductive heat flux to the surface. The temperatures predicted in the soil beneath Resolute are compared to measurements taken there at selected depths.

The following chapter (Chapter 4) is a discussion of the sensible and latent heat fluxes, and the surface energy balance model, which will diagnose the skin temperature, which is defined to balance the energy budget, a process that will involve all the terms of the surface energy budget, namely the upwelling and downwelling radiation, the conductive heat flux, and the latent and sensible heats. The upwelling radiation and the conductive flux are computed during the run of the model, using parametrizations and the knowledge that there must not be a net energy flux at the infinitesimal surface skin. The sensible heat and latent heat flux will be pre-calculated from balloon soundings, like the downwelling radiation. The surface balance model outputs the information sought by this study, a collection of all the surface energy fluxes as a function of time.

These time series of all the different energy fluxes are analyzed in Chapter 5, and their causes and effects are discussed. Of main interest is what insight, if any, can be gained about the role of the surface fluxes in the enhanced warming of the High Arctic. Of particular interest is what the effect that atmospheric radiation and the conduction from the sub-surface are having on the surface temperature.

CHAPTER 2

RADIATION

The greatest source and sink of energy for the surface is electromagnetic radiation. The spectrum of EM radiation important to the Earth's climate is divided conceptually into two sections: short-wave and long-wave. The separation is made to distinguish between the two common sources of this radiation, namely the sun and the atmosphere itself. The sun provides energy to the Earth in the form of short-wave radiation, which includes infrared, visible and ultra-violet light. The atmosphere emits radiation, which is for the most part in the infrared range.

During the winter in the High Arctic at Eureka, the sun goes down in October and does not rise again until the end of February. This greatly simplifies the number of variables in the radiative balance, by eliminating the need to include considerations of the short-wave. The presence of only long-wave fluxes allows its re-creation using only upper-air data, circumventing the need for data from such equipment as radiometers, which were not available in the Canadian High Arctic earlier than 2005.

To attain the goal of a reconstruction of the historical long-wave behaviour of the Arctic atmosphere, the SBDART radiative transfer code is used to diagnose long-wave radiative flux from the atmosphere to the surface. In the winter months, when the sun is below the horizon at all hours of the day, the long-wave flux makes up all of the total atmospheric radiative flux. The output reconstruction from the SBDART calculation will play a very important role in the understanding of the enhanced warming at Eureka and Resolute.

2.1 Background

Modeling of downwelling radiation is an important practice for surface balance studies in the absence of measurements. In the clear sky case, *Prata* (1996) derived a formula to simply calculate the downwelling irradiance using surface temperature and humidity measurements, and although it performs well for such a simple scheme, even in polar environments, it has an increased uncertainty of 12 Wm^{-2} compared to detailed radiative transfer codes. *Marty et al.* (2003) concluded that the calculations by MODTRAN, one of these more detailed codes, of clear sky irradiance agreed within 2 Wm^{-2} of measurements by a suite of upward facing pyrgeometers. These calculations used atmospheric temperature and water vapour data from radiosonde profiles.

Besides the clear-sky effects, an important part of the modeling of downwelling irradiance is the effect of clouds. *Curry et al.* (1996) estimated that during the Arctic winter, clouds have an average surface long-wave forcing of about 40 Wm^{-2} for 80° North. As was seen for Eureka specifically during the case study by *Doyle et al.* (2011), cloud forcing can be much smaller than this average value from case to case, as the ice clouds measured (and simulated using complementary radiative transfer calculations from SBDART) in this study had a radiative forcing between 10 and 30 Wm^{-2}, varying from cloud to cloud.

Both modeling and measuring radiation in the Arctic has proven to be a challenge. *Matsui et al.* (2011) discusses the troubles associated with operating instruments for measurement of long-wave irradiance, including frosting and riming which can cause the sensor readings to be indistinguishable from low-level clouds.

Just as the modeling of downwelling radiation has been used with success, so has the diagnosis of clouds from radiosonde profiles, at least at low latitudes. A statistical approach was used by *Arabey* (1975) to predict cloud amount based on temperature and dewpoint depression, and extended by *Chernykh and Eskridge* (1996) to predict cloud bases and tops as well. These studies use statistically-based criteria for different cloud amount categories ranging from 0-20% cloudy up to 80-100% cloudy, and the latter study showed success at predicting cloud height using the second derivatives of temperature and relative humidity. While this shows promise for predicting radiatively important clouds by a radiosonde method, it should be pointed out that the radiosonde sites used in Chernykh and Eskridge's paper were all in the continental United States, with vastly different atmospheric conditions than the High Arctic.

In the High Arctic, however, similar studies have been done to determine cloud structure based on radiosonde information. The approach of *Wang and Rossow* (1995) was to set a relative humidity threshold, above which a layer was predicted to be a cloud. Interestingly, this method used a relative humidity with respect to water threshold when the temperature was above 0° C and a relative humidity with respect to ice threshold when the temperature was lower, despite the fact that water clouds frequently appear in the Arctic below 0° C. *Jin et al.* (2007) detect clouds in the Arctic with reasonable success (67%), except in the detection of cirrus at temperatures below -40 C. It is thought that this high-altitude problem is due the difference in freezing mechanism that is brought out in the relatively less polluted high-latitude air. There are also issues at cold temperatures with the measurement of relative humidity, which introduce a "dry bias" (*Turner et al.*, 2003), especially at high altitudes in a wide range of different radiosonde devices (*Miloshevich et al.*, 2006) including those used at Eureka and Resolute. Dry bias is apparent in the comparison of precipitable water measured with radiosondes to that measured with a micro-wave radiometer. The dry bias is explained to occur because of lags in measurement response times at high altitudes, factory calibration techniques used prior to certain dates, and contamination of measurement devices by trapped gases other than water vapour (*Wang et al., 2002*), (*Miloshevich et al.*, 2006).

2.2 Model

2.2.1 SBDART

The downwelling long-wave radiation for this study is calculated using the radiative transfer code SBDART (*Ricchiazzi et al.*, 1998), which stands for Santa Barbara DISORT Atmospheric Radiative Transfer. This code takes as input profiles of water vapour, temperature, pressure, and ozone; along with concentrations of other greenhouse gases and cloud properties (which include cloud base and cloud top height, cloud particle effective radius, and cloud optical depth). The output for the purpose of the study is the spectrally integrated total downward irradiance.

The SBDART code was designed to be a versatile tool for use in many different types of radiative transfer calculations, including the budgeting of long-wave atmospheric radiation. SBDART is based on a collection of tested and reliable models and codes. The molecular

absorption is based on the models used in the LOWTRAN7 radiative transfer code, and the radiative transfer equation is solved using Stamnes' (1988) Discrete Ordinate Radiative Transfer (DISORT) method, which means that SBDART must operate on the plane-parallel assumption (see 2.2.1.1).

2.2.1.1 Physical Models

The atmospheric vertical profiles are defined from radiosonde measurements, and the trace gas concentrations other than ozone (section 2.2.4.2) are assumed to be vertically uniform. A precomputed set of parameters for the scattering by spherical cloud droplets is used, which are calculated using Mie scattering code. The parameters pre-calculated are the extinction efficiency Q_{eff}, the single-scattering albedo ω, and the asymmetry factor g, all as a function of wavelength of radiation and particle effective radii. The size distribution used is a modified gamma distribution.

The molecular absorption for SBDART is based on LOWTRAN-type band models to represent the effect of the entire set of atmospheric species important to radiative transfer. While these models have a low spectral resolution, they were derived from line-by-line calculations.

The numerical scheme used for integration of the radiative transfer equation is the Discrete Ordinate Radiative Transfer (DISORT) method (*Stamnes et al.*, 1988), which is used to solve plane-parallel radiative transfer in an atmosphere which contains vertical inhomogeneities. The plane-parellel assumption is valid provided that the scale of horizontal variability is larger than the vertical scale of interest. For the purposes of this study, this will be true except in the case of partially cloudy skies, but the handling of this discrepancy is discussed in 2.2.3.2.

2.2.1.2 SBDART Long-wave Experiments

While comparison of SBDART-calculated spectral radiances with those measured by an atmospheric emitted radiance interferometer (AERI) in case studies shows a 3% discrepancy (*Ricchiazzi et al.*, 1998), it shows success in predicting broad-band irradiance. In the case-study of water vapour intrusions in the High Arctic by Doyle et al. (*Doyle et al.*, 2011), SBDART was used to calculate the change in downwelling long-wave irradiance at the surface due to changing cloud, water vapour, and temperature fields (This portion of

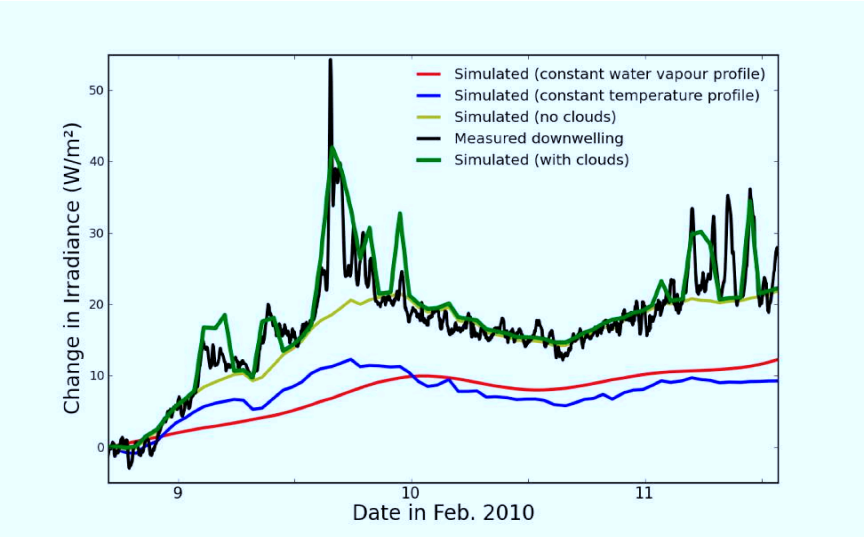

Figure 2.1: Case study adapted from Doyle et al (2011). The black line is the change in irradiance measured by the NOAA pyrgeometer at Eureka. The other lines are simulated changes in irradiance for the full (clouds included) simulation (green line), the cloudless simulation (yellow line), the temperature effect (red line) and the water vapour effect (blue line). The temperature/water vapour effects were calculated by holding the water vapour/temperature profiles constant at their starting values while allowing the temperature/water vapour to vary.

the paper was completed as a part of this work). The atmospheric vertical temperature and pressure profiles for this study were supplied by radiosonde measurements interpolated to give an hourly data-set. This was combined with hourly integrated water-vapour and cloud profiles obtained from the CANDAC Rayleigh-Mie-Raman Lidar (CRL) that is stationed in Eureka, to create a simulation of the changing radiative environment over a three day span. The modeled change in irradiance is compared to that measured by a co-located pyrgeometer, and shows very good agreement (Figure 2.1).

Further, the total change in irradiance was decomposed into three contributions: the cloud, temperature, and water vapour. The latter pair are represented by the red (temperature) and blue (water vapour) lines, while the cloud forcing is the difference between the green and yellow lines. The total change in irradiance is, to within 1 W m^{-2}, the sum of these three effects. This study provides confidence in the ability of SBDART to simulate winter downwelling fluxes in the High Arctic environment, and in the power of the method of decomposing the total radiative forcing into distinct sources.

2.2.2 Radiosonde Profiles

2.2.2.1 Radiosonde Water Vapour, Temperature Profiles

Upper air data has been recorded every 12 hours in Eureka since 1948. The data set used is from Environment Canada's upper air archive, which starts in 1961, and is made up of measurements by radiosonde balloons released from the Eureka weather station. The radiosondes measure pressure, temperature and relative humidity as they rise buoyantly, and therefore give altitude profiles of each of these variables. The great benefit of such measurements is that they contain the vertical structure of the temperature and humidity fields in the atmosphere, which are major contributors to the long-wave radiative flux. Unfortunately, in the beginning months of 1994, Environment Canada switched radiosonde manufacturers, and so broke the upper air record into two inconsistent (*Miloshevich et al.*, 2006) sections, 1964-1993 and 1994-present (Figure 2.2). For this reason, only the radiosondes from the latter time period are used in the current work.

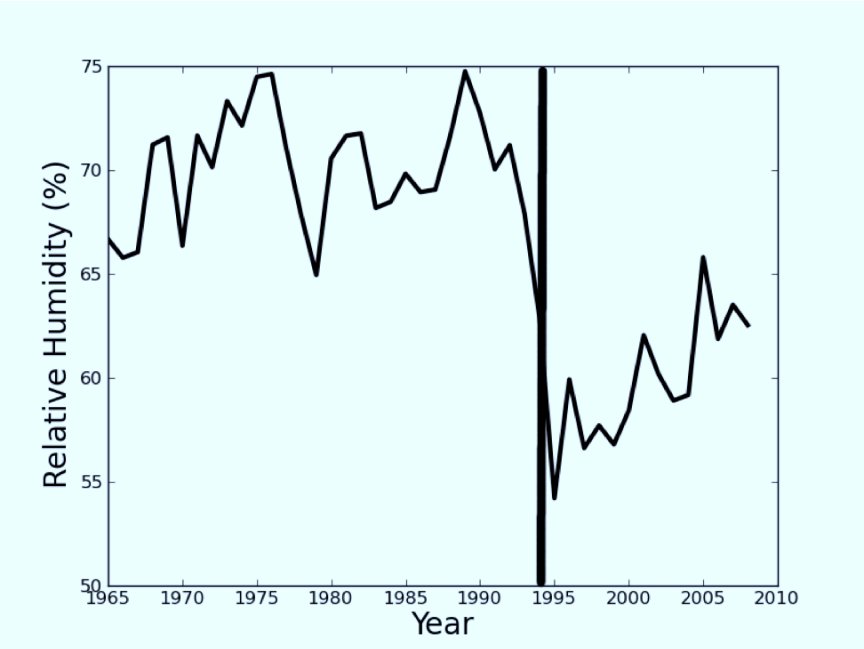

Figure 2.2: Winter averaged tropospheric average relative humidity at Eureka for the time period 1965-2009. Note the drastic change between the years 1993 and 1995. The radiosonde equipment transition (vertical line) occured on January 18th 1994 (personal correspondence).

2.2.3 Radiosonde Clouds

Since the only upper air data that is available throughout the entire period from 1994 to present is the Environment Canada radiosonde data-set, the clouds for the long-wave radiation reconstruction must be retrieved from said atmospheric soundings. In terms of cloud formation and variables measured by the radiosondes, clouds should appear at altitudes and times where the relative humidity is greater than 100%, provided that the appropriate condensation nuclei are present. It is therefore reasonable to assume that clouds should be in some way retrievable, at least in a climatically appropriate way, from the properly calibrated radiosondes.

2.2.3.1 Clouds From Radiosonde Retrieval

A method is used for retrieving cloud altitudes and thicknesses from radiosonde relative humidity profiles, which bases its predictions on a combination of a given radiosonde's relative humidity profile and a statistically derived relative humidity threshold profile. At altitudes where the measured relative humidity is higher than the corresponding threshold value, a cloud is predicted. There are two different thresholds derived for cloud prediction, one for water clouds and one for ice clouds. The former is a threshold in the relative humidity with respect to water, and the latter the relative humidity with respect to ice. The relative humidity over ice (RH_{ice}) is always higher than that over water (RH_{water}) at temperatures below 0 degrees Celsius, leading to a higher value for the RH_{ice} threshold since there are many more instances of super-saturation with respect to ice than to water.

The tuning of the thresholds is done by selecting the threshold value at each altitude which results in the same cloud frequency for the months October to February as that observed by the Arctic High Spectral Resolution Lidar (AHSRL). This is a NOAA-operated instrument that acquired data at Eureka between the years 2005 to 2010, which actively measures backscatter and depolarization ratio profiles of the atmosphere by ranging with a 532 nm laser. To match the cloud frequencies, all the points in time at which there is available data from both radiosonde and lidar are selected to form a comparison data set. From these data, a cloud frequency is calculated at each altitude by dividing the number of instances with a cloud present ($\mathrm{N}_{cloud}(\mathrm{z})$) by the total number of points in the collection of data ($\mathrm{N}_{total}(\mathrm{z})$). The resulting calculated frequency profile is used as an ideal to which the radiosonde method can be matched using a least-squares method described below.

$$\omega_{lidar}(z) = \frac{N_{cloud}(z)}{N_{total}(z)} \tag{2.1}$$

The relative humidity threshold is given two degrees of freedom which will be allowed to vary independently of each other, and which will be adjusted to best fit the ω_{lidar}(z) profile. The first of these (α) defines the constant relative humidity threshold from the surface to 5 km, while the second (β) defines the threshold at 10km, which is reached after linearly increasing with altitude starting from 5 km. 5 km is chosen for this point of change because it is the altitude at which cloud behaviour significantly changes, both in terms of optical properties (Figure 2.5) and relationship between cloud frequency and relative humidity. A cloud profile can then be generated for each radiosonde, and the frequency at which this method predicts clouds to be at each altitude can then be calculated by the same method as used for the lidar above (also for the winters of the time period October 2006 - March 2009), giving $\omega_{radiosonde}$(z). A least squares fit is performed which calculates a best value for α (α_{best}) which minimizes the difference between ω_{lidar}(z) and $\omega_{radiosonde}$(z) below 5km. Another least squares fit can then be done using α_{best} and varying β to calculate β_{best}, which minimizes the difference above 5km. The result of this tuning and its comparison to the AHSRL measurement is presented in Figure 2.3.

An example radiosonde cloud retrieval is shown in Figure 2.4. At the time of this particular sounding, the relative humidity with respect to ice had a value above the threshold in two different altitude ranges, the first below 500 m and the second between 1.5 km and 2 km. This sounding was chosen as an example because it also contains a region where the relative humidity with respect to water was above its threshold, leading to a predicted profile of one ice cloud below 500 m, where only the RH_{ice} threshold is broken, and a water cloud just below 2 km, where both thresholds were broken. The comparatively high RH_{ice} threshold at the higher altitudes is required to suppress the over-prediction of very high clouds; in the region where it is extremely cold, the relative humidity over ice is accordingly very high, but there is less likely to be ice nuclei available for cloud formation, and the radiosonde's humidity measurement is less reliable (*Miloshevich et al.*, 2006).

Once the cloud altitudes and thicknesses are predicted using the above method, their optical depths must still be obtained. A thorough study of variables showed no usable relationships with optical depth or extinction (not shown), and so an average extinction coefficient profile is integrated over the altitude range of a cloud to obtain the cloud's

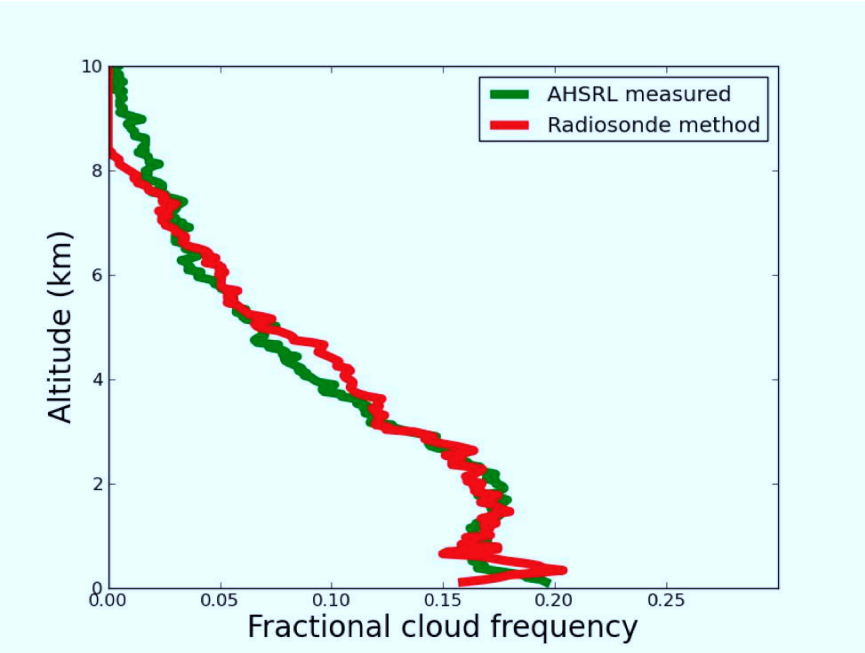

Figure 2.3: Frequency comparisons between the AHSRL clouds (green) and the radiosonde cloud method clouds (red) as a function of altitudes during winter for the time period of Oct 2006 to Mar 2009. Frequencies were calculated as the fraction of the total number of profiles which contained a cloud at each altitude. Only data points corresponding to reasonable measurements were used (i.e. lidar profiles above heavily extinguishing low clouds were thrown out). This lack of data above highly-extinguishing low clouds would only introduce a bias if there is correlation between presence of low clouds and high clouds.

optical depth. Figure 2.5 shows this calculated mean profile for ice clouds, which was obtained by averaging the extinction of clouds measured by the AHSRL at each altitude for all winter radiosonde times between the years 2006 to 2009. The extinction profile shows a higher value for lower ice clouds (3x10^{-4} m^{-1}), and a lower value for the high, thin ice clouds that appear above 5 km (10^{-4} m^{-1}). For water cloud extinctions, a single value of 5 x 10^{-4} m^{-1} was calculated from the AHSRL data, and is used for water clouds at all altitudes.

2.2.3.2 Partial Cloudiness

Since there are often partially cloudy days (see Figure 2.6), which will have a different longwave forcing than days of whole-sky clouds, a simulation of partial cloudiness will be necessary. The way this is done for this study is to run two separate irradiance simulations

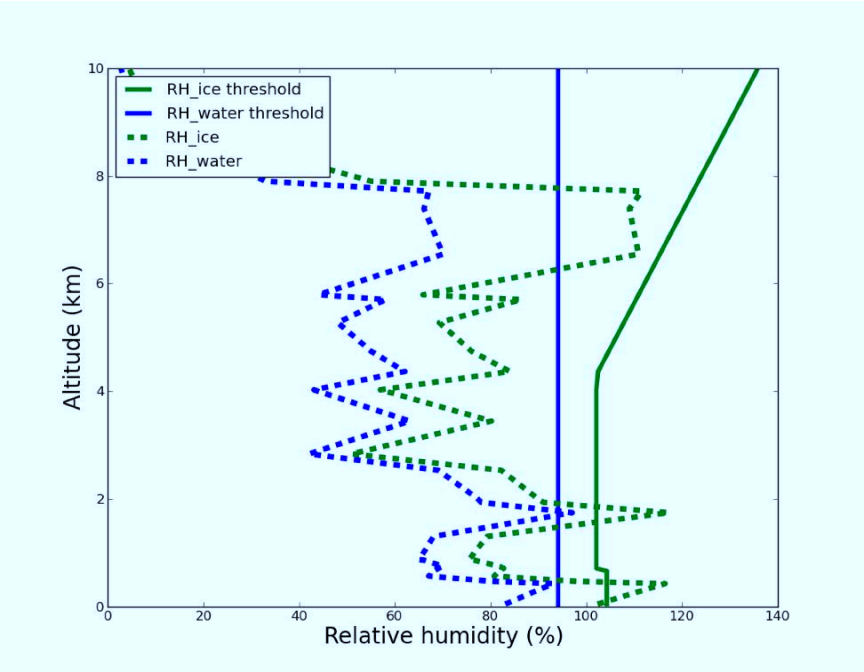

Figure 2.4: An example radiosonde cloud retrieval from the 2008-11-01T00 radiosonde profile. The solid blue and solid cyan lines are the thresholds of relative humidity with respect to water and ice, respectively. The dashed blue and cyan curves are the measured relative humidity with respect to water and ice. When the measured value breaks the threshold had any altitude, a cloud is predicted, with water clouds taking precedent. In this example, a thin water cloud is predicted at 2 km and an ice cloud is predicted near the surface.

using SBDART, one with only clear skies at every point in time and another with the full cloud prediction. These two runs are then combined in the case of partial cloudiness to achieve the final predicted irradiance. The formula to combine the two is a simple weighted mean:

$$DW_{final} = (1 - CF)DW_{clear} + (CF)DW_{cloudy} \tag{2.2}$$

where CF is the surface observed cloud fraction. Note that the equation will return the fully cloudy irradiance when the cloud fraction is equal to 1, and fully clear irradiance when $CF = 0$. The frequency of occurance of different cloud fractions is plotted in Figure 2.6.

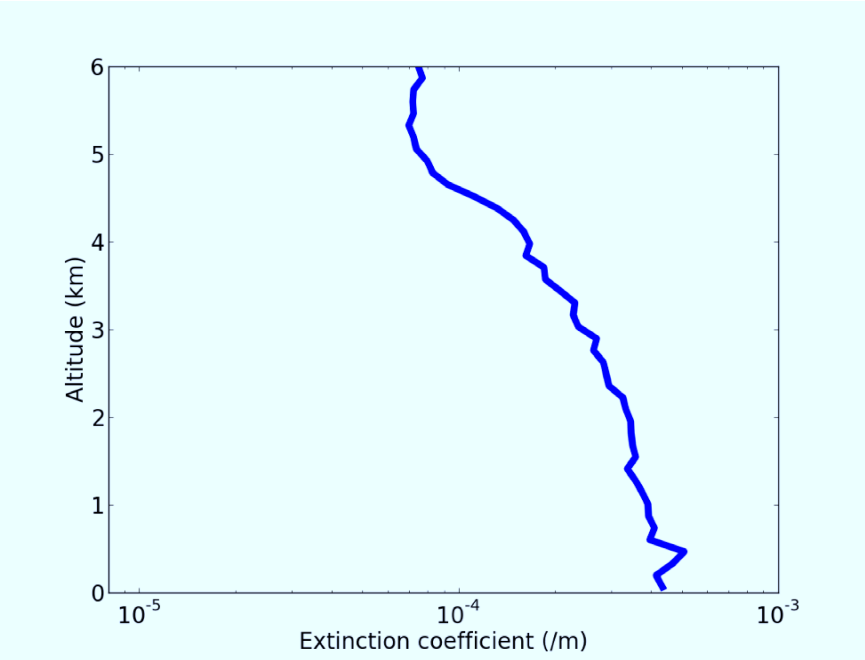

Figure 2.5: The mean extinction coefficient of ice clouds as a function of altitude calculated from AHSRL backscatter data. The average extinction at all altitudes containing clouds in all profiles in the period Oct 2006 to Feb 2009 is computed to achieve this profile. As an example, an ice cloud predicted between 1 and 3 km would have roughly an optical depth of one.

2.2.3.3 Radiosonde Cloud Method Irradiances

While the predicted cloud frequency profile was tuned to be in good agreement with measurement, the result of interest is the predicted downwelling irradiance predicted by a combination of the radiosonde clouds (RSC) and the SBDART code. This radiation prediction is accomplished by feeding the radiative transfer code with the predicted altitude and optical depth of the clouds in the profile, and assuming an effective radius for cloud particles. An effective radius of 60 μm is used, but the far-infrared radiative transfer is fairly insensitive to this assumption between effective radii of 20 μm to 120 μm. As a data-set for comparison, the SBDART code is also run using cloud properties from the AHSRL, which measures the optical depth and cloud altitude range directly. The two sets of predictions (RSC- and AHSRL-derived irradiances) for radiosonde times when the AHSRL or RSC method show a cloud (or clouds) in the sky in the winters 2006-07 to 2008-09 are plotted in Figure 2.7. The clear sky cases are not plotted, as these are identical using these two methods. The agreement between the two is good, with a mean error less than 10 %, and

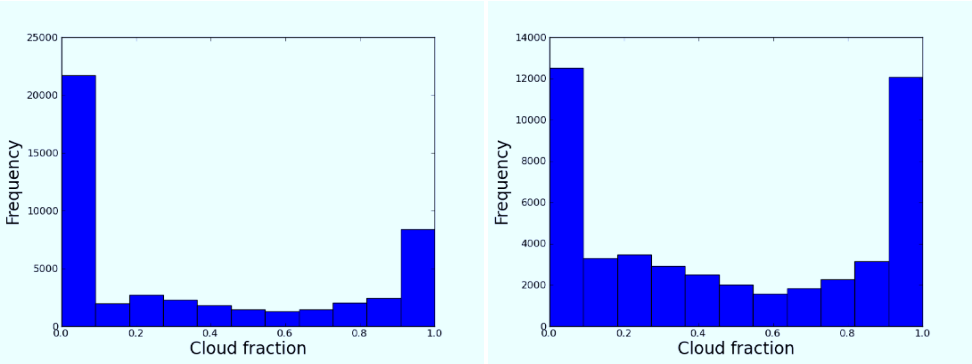

(a) Eureka (b) Resolute

Figure 2.6: Histograms of cloud fraction for (a) Eureka and (b) Resolute for winters in the time period 1994 and 2008. Cloud fractions are reported in tenths from 0 to 1, giving the 11 bins in each figure.

more importantly for large time-scale reconstruction a negligible mean bias. In a climate sense, random errors are relatively unimportant when compared to systematic biases because the seasonal time-scale variation will be insensitive to the former but will enhance the latter. This situation is analogous to a casino that can be assured a steady payoff from its games of chance because of the slight "house"-ward bias of the odds for the games, while being completely incapable of predicting the outcome of any one hand of blackjack.

In the same way that the RSC-modeled irradiance can be compared with its lidar-derived counterpart, it can also be compared to measurements of irradiance made at Eureka. Figure 2.8 shows this comparison, with the measurements coming from a skyward facing pyrgeometer, which measures the broad-band downwelling infrared irradiance. This comparison does show a respectably high correlation coefficient (0.81); it also shows a few interesting features, the most obvious being the low bias by the model of 8 W m^{-2} on the clear, low-irradiance days (blue dots). This is thought to be caused by a frosting issue that this particular pyrgeometer suffers from, where a thin layer of frost on the instrument contributes a small amount of added irradiance. The second feature that catches the eye in this comparison is the even lower bias as the measured irradiance increases (red dots). This bias was not present in the lidar comparison, but is possibly a result of the small number of data-points in the comparison, or a manifestation of the effect of thick frosting that is discussed by *Matsui et al.* (2011) as creating falsely cloud-like irradiances. Because of

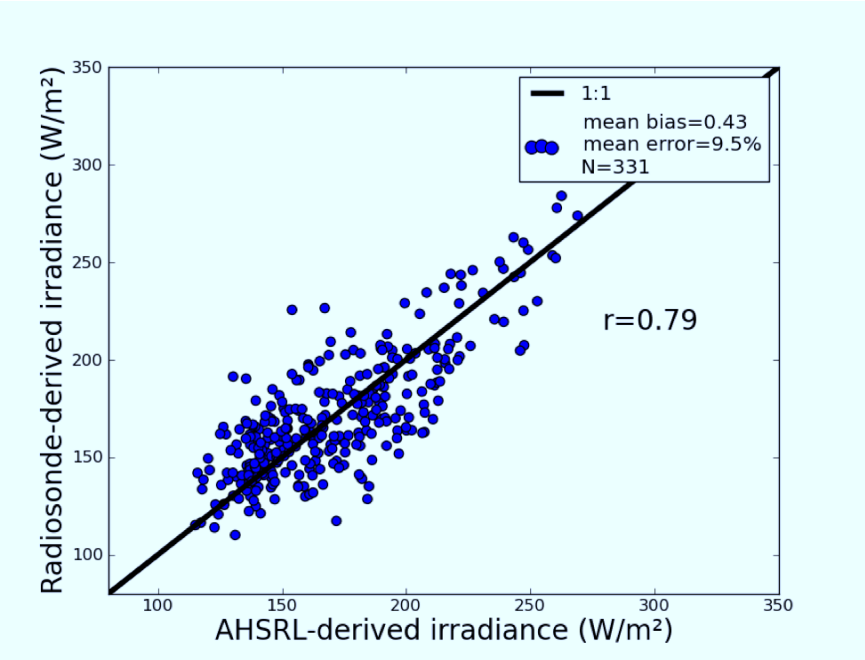

Figure 2.7: Comparison of RSC cloudy sky irradiance with AHSRL cloudy-sky irradiance. This scatter plot has points which are individual soundings whose location in the space are determined by their predicted downwelling irradiance using AHSRL data and SBDART (along the x-axis) and using the RSC method and SBDART (along the y-axis). Only soundings in which the lidar or the RSC method returned a cloud were used. The scatter shows negligible bias and a mean error of less than 10%.

these possibilities and the success of the comparison shown in Figure 2.7, this cloud prediction method is deemed to be adequate for the purpose of reconstructing the downwelling irradiance from radiosondes.

2.2.4 Greenhouse Gases and Ozone

Infrared radiative transfer in the atmosphere is governed almost completely by absorption and emission, as opposed to the shorter wavelength regions, which have a strong scattering component. By Kirchoff's law, a substance's relative ability to absorb is equivalent to its ability to emit, and thus the strongly absorbing gases and particles that inhabit the atmosphere have the greatest impact on the behaviour of long-wave radiation. The focus of this section is the effect of the absorbing gases, of which there are many, but only those with the largest impact (excepting water vapour) will be discussed below.

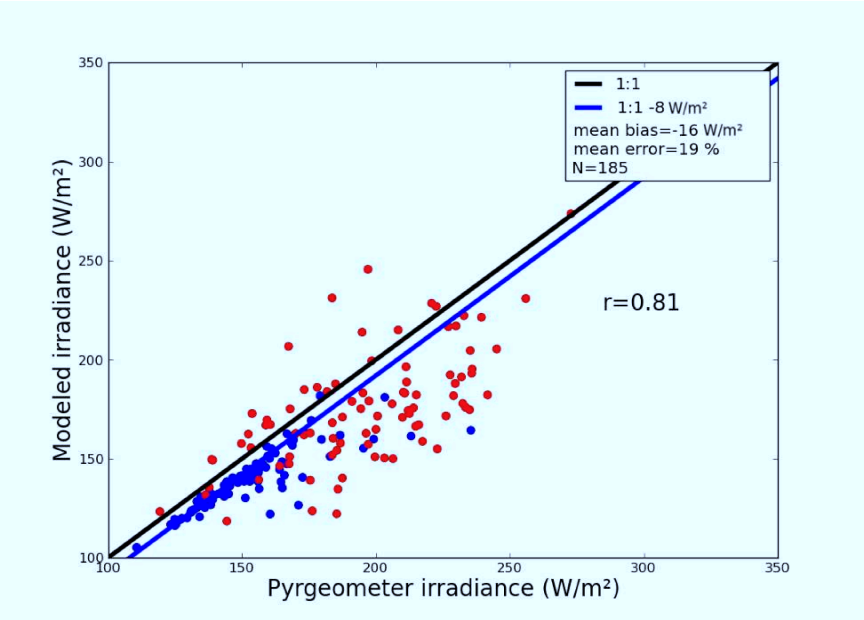

Figure 2.8: The same as Figure 2.7, but using the pyrgeometer-measured irradiance (x-axis) and the RSC method irradiance (y-axis) for both clear (blue) and cloudy skies (red). This comparison shows an offset of 8 W m^{-2} (blue line) for low irradiance soundings, which is thought to be the effect of light frosting on clear, cold days, and a further low bias of 8 W m^{-2} overall. This is potentially due to a frosting and riming issue that gives the illusion of cloudy skies to the pyrgeometer [Matsui 2011].

2.2.4.1 Trace Gases

A substantial proportion of the infrared region of the spectrum contains the absorption signatures of three important long-lived gases, namely methane (CH_4), nitrous oxide (N_2O), and carbon dioxide (CO_2). These gases have atmospheric lifetimes ranging from more than 10 years (N_2O) to hundreds of years (CO_2), and so are very well-mixed vertically and horizontally and their effect can be diagnosed from a single quantity, their concentration. The concentrations of these gases have been increasing since the 1970's, and this increase results in a positive radiative forcing.

Simple experiments with the concentrations of these gases using SBDART show that the effect of the increased abundance of the long-lived gases has no major effect on the scale of the changes that are seen in this study. While the gas concentrations are modeled to increase as they did globally over the time period of interest, their winter radiative effect was very small, estimated as less than 0.2 Wm^{-2}.

2.2.4.2 Ozone Profiles

Unlike the longer-lived greenhouse gases, ozone (O_3) is not vertically homogeneous in the atmosphere, and thus the shape of its vertical distribution profile has an impact on the long-wave radiative transfer. The vertical ozone profile is obtained from ozonesondes, which are launched from the Eureka weather station at week- to day-long intervals, depending on the time of year. The change in profile shape is due to ozone-related photo-chemistry, which occurs when the sun rises up at the end of the dark season, and ceases at the end of the light season.

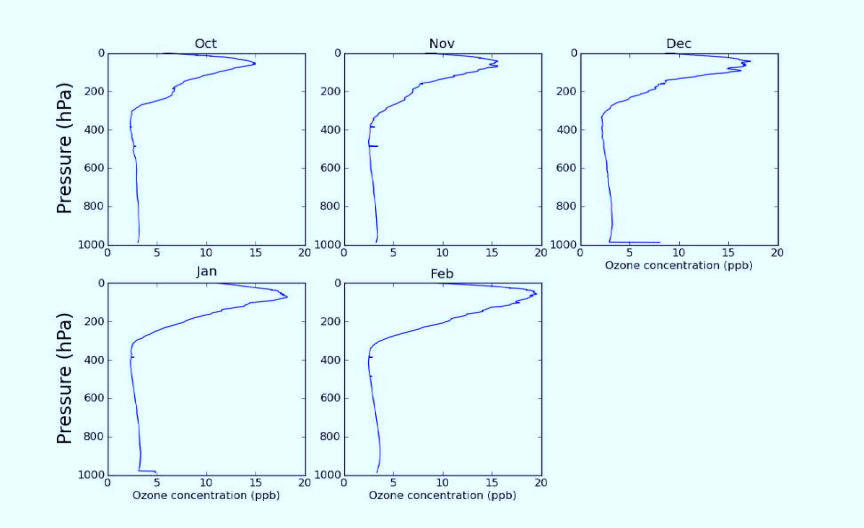

Figure 2.9: Mean profiles of ozone concentrations as a function of pressure for each winter month, calculated from all available ozonesondes from 2005 to 2009.

The ozone profile for each month of the winter is attained by calculating the mean ozone profile from all ozonesondes in that month between the years 2005 to 2009. As changing ozone is not the concern of this study, and as the available data-set is fairly restricted in time, the effect of inter-annual variability or trends of ozone on the downwelling irradiance is not considered. Figure 2.9 shows the calculated average ozone profile as a function of pressure for each month. Of note is the increasing concentration of ozone aloft as the winter progresses, reaching a maximum in February before the sun's rays return to deplete ozone photo-chemically.

2.2.5 *Upwelling Radiation Parametrization*

The parametrization for the upwelling radiation (UW) for future use in the surface energy balance is simply the Stefan-Boltzmann law, which relates the irradiance from a surface to its temperature. By the definition of surface balance, this temperature at which the surface skin is radiating is the skin temperature, T_s. The Stefan-Boltzmann law has the form

$$UW = \epsilon \sigma T_s^4, \tag{2.3}$$

Where σ is the Stefan-Boltzmann constant, with a value of 5.67 x 10^{-8} $\mathrm{Wm^{-2}K^{-4}}$, T_s is the skin temperature in K, and ϵ is the emissivity of the snow that covers the winter surface. To simplify the parametrization, a constant emissivity is used, taking a value of 0.97, which is typical of snow (*Kondo and Yamazawa*, 1985).

2.3 Reconstruction

With the model for the prediction of downward irradiance using radiosondes described above, a reconstruction of past irradiances can be performed. In the following subsections, two locations were chosen for the reconstructions, Eureka and Resolute. To reconstruct the time-series for winter downwelling radiation, each available radiosonde was used, giving between 220 and 240 data points per winter. In the following sections, winter averages are used, with winter of a given year being defined as the period between October 20^{th} of the year and March 1^{st} of the following year.

2.3.1 *Eureka*

Over the time period of winters 1994-95 to 2008-09, Eureka shows a marked increase in surface downwelling irradiance. The trend in this quantity is a significantly positive one, with a value of 7.9 $\mathrm{Wm^{-2}decade^{-1}}$ and an uncertainty in the slope of 3.7 $\mathrm{Wm^{-2}decade^{-1}}$. Figure 2.10 shows the time series for downwelling long-wave irradiance in black, with a dashed line showing the linear fit of these data. The straight black lines are the bounding slopes of the 95 percent confidence interval, meaning that there is a 95 percent chance that the actual slope falls somewhere between these two lines.

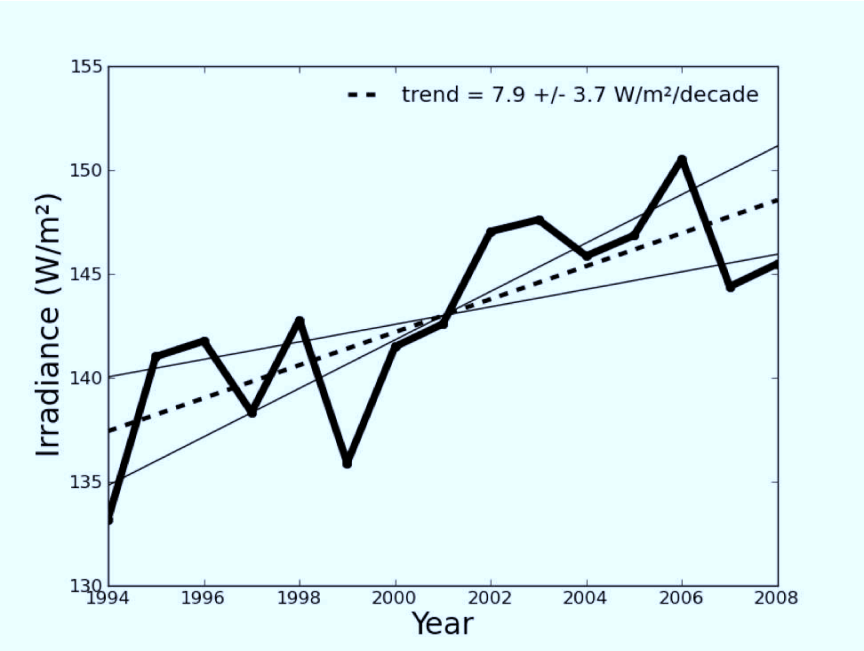

Figure 2.10: Reconstruction of downwelling longwave radiation at Eureka. Values are averages over the whole winter. The winter labeled YYYY starts in October YYYY and goes until March YYYY+1. The dashed line is a linear fit for the data, and the straight, thin black lines are bounds of the 95 percent confidence interval of the fit. The slope of the line of best fit is 7.9 ± 3.7 $\mathrm{Wm^{-2}decade^{-1}}$.

2.3.2 Resolute

Resolute's downwelling long-wave irradiance behaves in a similar way, showing an increase of 14.8 $\mathrm{Wm^{-2}decade^{-1}}$ with an uncertainty of about half of that slope (6.7 $\mathrm{Wm^{-2}decade^{-1}}$). Figure 2.11 shows this behaviour and its uncertainty, in the same way that Figure 2.10 does for Eureka. The increase is larger than that at Eureka, but it comes with a larger uncertainty, meaning that there is a chance that the underlying behaviour is actually quite similar. The causes for the increase in downwelling irradiance for both Eureka and Resolute will be discussed in Chapter 5, but for now it will suffice to note that it is rising over the time period, with statistical significance.

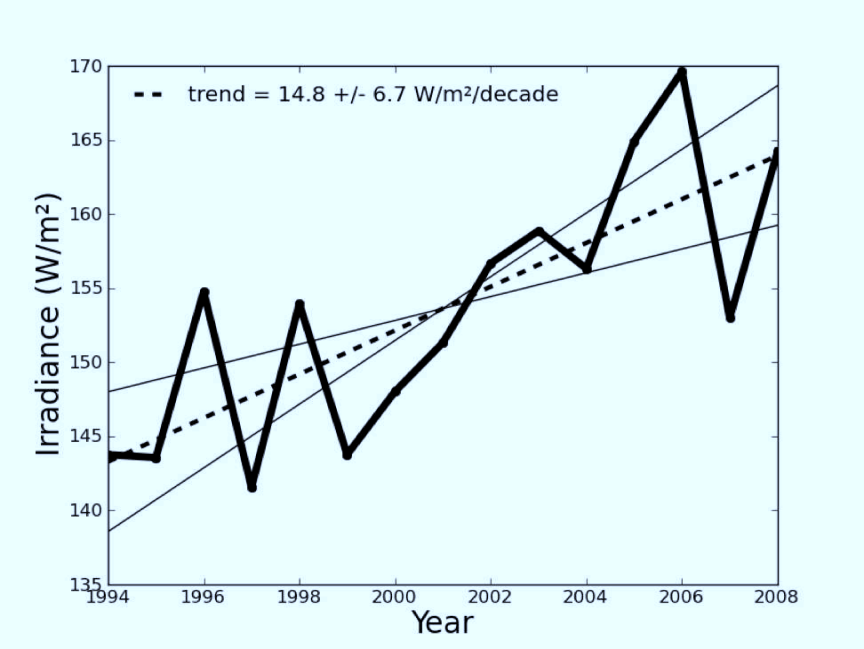

Figure 2.11: Same as Figure 2.10, but for the reconstruction of downwelling longwave radiation at Resolute. The slope of the line of best fit is 14.8 ± 6.7 $\mathrm{Wm}^{-2}\mathrm{decade}^{-1}$.

CHAPTER 3

GROUND CONDUCTIVE FLUX

While the interaction of the surface with the atmosphere through radiation is an important component of the energy transfer related to climate, it is not the only way that the surface climate is forced. Neither is the atmosphere the only changing body that affects the surface. The other important source of energy to the Arctic surface is the snow and soil beneath it. The ground below has a much greater heat capacity than the atmosphere above, and provides a steady supply of energy throughout the winter through the transfer of energy by conduction. The soil beneath the surface provides a medium through which conduction to or from the surface can occur and plays an important role in determining the behaviour of the surface skin temperature.

3.1 Background

The vulnerability of permafrost to climate change is discussed by *Jorgenson et al.* (2010). They conclude that permafrost degradation is possible for locations of mean annual air temperatures down to -20° C, meaning that Eureka and Resolute fall in this vulnerable category. Although the study displayed in that paper was for a variety of soil types, such detail will not be possible in the current work, as soil property data is unavailable for the locations of interest.

Literature is available, however, on the general conductive properties of soil and snow. *Fukusako* (1990) reviews the important conductive properties for snow, namely the thermal conductivity and diffusivity. The conductivity is found to have a strong dependence on

snow density, which gives a broad range of conductivity values to use for Eureka's and Resolute's snow covers (0.15 $Wm^{-1}K^{-1}$ to 0.4 $Wm^{-1}K^{-1}$). This is in agreement with the study by *Aggarwal et al.* (2009) which provides a similar range of snow conductivities.

Analysis by both *Weller and Schwerdtfeger* (1970) and *Ling and Zhang* (2004) show that sub-surface temperature fluctuation amplitudes shrink with depth, to a point where the temperature is effectively constant. This depth is below 10 m for Weller and about 15 m for Ling and Zhang. Furthermore, Ling and Zhang use a full conduction scheme driven by surface energy balance to simulate the sub-surface temperature profile. Their success, while using a basic set of parametrizations to drive their model and a coarse snow thickness scheme, is encouraging for the ability of the current work to reconstruct reasonable historical heat flux from below the surface. Ling and Zhang cite snow density as playing a major part in uncertainty for surface-driven conduction models.

3.2 Diffusion Model

The conduction model used in this study operates by solving the diffusion equation for temperature for a given temperature depth profile, and using the result to make a prediction of how the temperature will change in time. This model will supply the sub-surface temperatures which, in combination with the temperature of the surface skin, will give both a diagnosis the conductive flux to the surface and a prognosis of the skin temperature's behaviour. The 1-D diffusion equation for temperature is

$$\frac{dT}{dt} = \kappa \frac{d^2T}{dz^2} \tag{3.1}$$

where T is the temperature at a given depth z, and κ is the thermal diffusivity of the medium of conduction (e.g. soil or snow). To solve this, the numerical ODE solver from python's *scipy* package is used, which is based on the FORTRAN numerical solver LSODA (*Hindmarsh*, 1980).

The model will be run in two distinct modes, for two distinct purposes. The difference between the two will be the surface boundary condition used. The first mode will be the annual mode, where the model is run with a surface boundary condition where the skin temperature is a function of the air temperature, with the specifics of this function described

in the following subsection. With this annual mode, the goal will be to capture the long-timescale behaviour of the soil and permafrost temperatures. For example, a hotter than average summer will warm the soil deeper down. In the annual mode, the model will resolve the effect of these hotter/colder seasons, while not resolving well the day-to-day or hour-to-hour temperature variations in the active layer. The reason for capturing the large-scale inter-annual behaviour in the annual mode will be to initialize the second mode, which will run a much more detailed winter simulation, but will require the deep temperature information from the annual mode to initialize it.

This second, more detailed mode, which will be referred to as the winter mode, is run with a more complicated top boundary condition, where the skin temperature is determined by solving the surface energy balance equation, which will be discussed in the following chapter. In this mode, the short-timescale interactions of all the surface meteorological variables and the radiation from the atmosphere will be resolved, and a detailed synoptic-scale re-creation of the active layer will be achieved. It is important that these small scale variations in soil temperature are captured, so that the surface conductive flux can be better diagnosed.

3.2.1 Surface Temperature Boundary Condition

To solve the diffusion equation forward in time, there must be boundary conditions set at the top and bottom of the temperature profile. For this model, the bottom boundary condition is the simplest one, that the rate of change of the temperature there is negligible. This assumption is essentially an assertion that there is a depth at which the temperature is constant year-round. The top boundary condition will therefore be the one that drives the underground temperature behaviour, and is considerably less simple. This boundary condition can be given by defining a temperature for the surface skin, which is the infinitesimally thin top layer that is a part of the modeled conduction. Two different methods for defining the skin temperature will be used in this study; the first being a skin temperature value calculated from surface energy balance, to be discussed in the next chapter, and the second being a skin temperature based on the air temperature measured above the surface at a given time, to be discussed below.

In the annual mode, where surface energy balance is not solvable by the methods used

in this study due to the presence of solar radiation in the summer, an alternate and preferably simpler method for driving the underground temperature fluxes must be used. It is important for the study of the winter conductive flux to have effects even from the summer temperatures because the sub-surface temperatures are slowly varying, and so a hotter than average summer, for instance, will result in the soil releasing some of that extra thermal energy during the winter.

The simplest way to capture this behaviour would be to define the skin temperature for the annual mode as being equal to the air temperature. That way, hotter/colder summers will lead to hotter/colder starting points in the soil temperature profile for the following winter. To first order, this is exactly the consideration that is required to properly initialize the winter mode conduction calculations, but the complicating factor that must be addressed is the fact that the skin temperature is not the same as the air temperature. In fact, there are systematic ways in which the two differ, and these can be easily quantified to obtain a working model for the annual mode skin temperatures.

3.2.1.1 Summer Skin Temperature

The skin for the summer months (say the months without snow cover), is the level at the interface between soil and atmosphere. During the summer, this skin temperature is greatly affected by the presence or lack of solar irradiation. On cloudy days where the incoming solar beam is greatly attenuated, the skin and air above it are likely to have very similar temperatures. On the other hand, on clear summer days the soil is able to absorb most of the much greater incoming solar energy and this creates a large increase in surface skin temperature, which is much more weakly mimicked by the air temperature. On clear summer days, therefore, the measured air temperature can underestimate the skin temperature. MODIS (Moderate Resolution Imaging Spectroradiometer) instruments frequently overpass the Arctic on-board the satellites Terra and Aqua, and retrievals of skin temperature are made using the split-window algorithm *Wan and Dozier* (1996), using estimated emissivities from land cover types. Figure 3.1 shows a comparison between the surface observed air temperature and the MODIS-measured skin temperature at Eureka as a function of time for the summer of 2005. As this plot shows, the clear-sky skin temperatures range from about 5 degrees to upwards of 15 degrees warmer than the air temperatures. When the clear- to cloudy- sky ratio is factored in, this leads to an average skin temperature offset of

+5 degrees from the air temperature when the snow-cover is gone from the surface, which is the value used to define the summer skin temperatures for the annual mode.

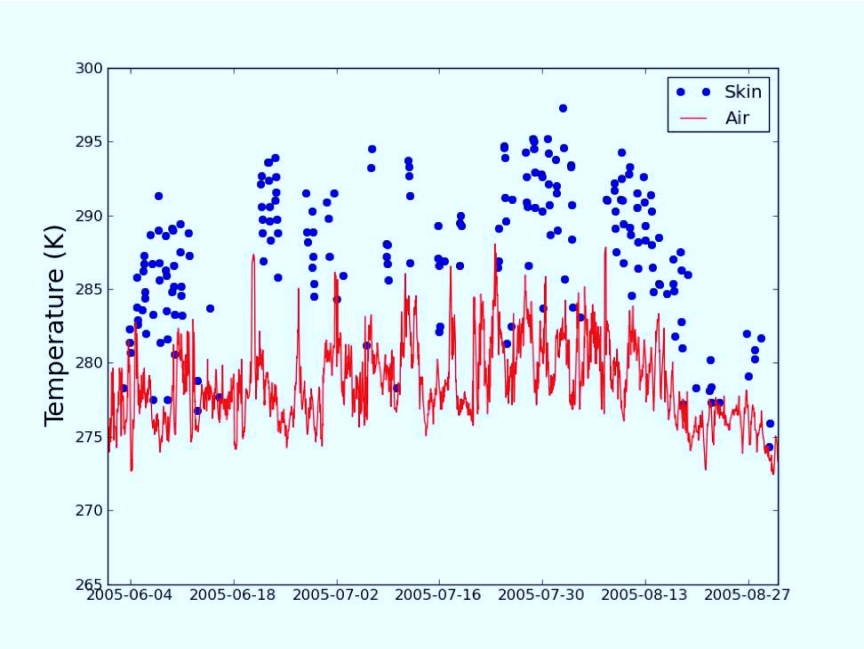

Figure 3.1: Eureka surface observed air temperatures (red line) and MODIS-derived skin temperatures (blue points). The MODIS retrieval of skin temperature is only available during clear skies, so time periods without blue points correspond to cloudy skies. The average value of skin-air difference over the clear skies of the entire summer is + 8.5 K. With a temperature difference assumed to be about 0 K on cloudy days, this gives a summer all-sky average of + 5 K for the skin-air temperature difference.

3.2.1.2 Winter Skin Temperature

During the winter in the High Arctic, the opposite skin temperature effect to that in the summer takes place. With the complete lack of solar energy at the surface, the skin is significantly colder than the air on clear days, when it can freely radiate energy away. On cloudy days, the increased downwelling long-wave radiation mitigates this effect, but on average, the skin during the winter is at least a couple of degrees colder on average than the measured air temperature. In the winter of the annual mode simulation, a skin temperature offset of -3 degrees from air temperature is used to drive the model from above, as this difference is an average feature of the winter mode model runs under many conditions.

Table 3.1: Skin temperature definitions by season

Season	Date range	T_s definition
summer	June 1 - Sept 1	T_{air} + 5 K
transition	Sept 1 - Dec 1, Mar 1 - June 1	min(273.15 K , T_{air}) if snow present
winter	Dec 1 - Mar 1	T_{air} - 3 K

3.2.1.3 Transitional Season Skin Temperature

With the sun-filled and dark seasons addressed above, the remaining point of concern for the annual mode top boundary condition is the skin temperature during the transition months, where there is snow remaining on the ground, when the sun rises and sets daily, and ambient temperatures are in the process of changing from one extreme to the other. During this transition, particularly in the winter to summer transition, the air temperature can rise above 273.15 K while there is still snow on the ground. Since it would be unphysical to define the snow surface as having a temperature greater than its melting point, 273.15 K is defined as the maximum temperature for the snow surface. The effect of adding this stipulation is small, as the time period between higher temperatures and snow melting away is small.

Table 3.1 shows a summary of the skin temperature definitions by season for the annual mode.

3.2.1.4 Snow Depth

As the "surface", as it is defined in this study, is at the soil-air interface in the summer but the snow-air interface when there is snow, the depth of the snow at any given time will be an important variable to account for. This is because the snow is a good thermal insulator, due to both the added distance it creates between a given depth and the surface (i.e. top of snow layer), and its relatively low thermal conductivity. Figure 3.2(a) is a plot of the average winter snow depth at Resolute, which is measured by meteorological technicians at a single representative location for the duration of snow cover, and shows a very strong variability from year to year. Without capturing this in the simulation, very large errors would be present each winter. Figure 3.2(b) shows a similar variability, but also

that Eureka tends to have less snow cover than Resolute. This fact should lead to decreased insulation of energy release from below during Eureka's winter.

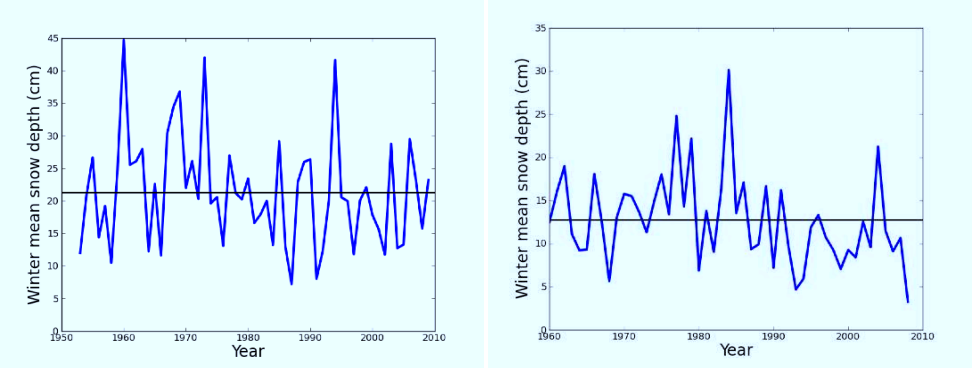

(a) Resolute (b) Eureka

Figure 3.2: Average winter snow depths for a) Resolute and b) Eureka for all years on record at Environment Canada for each site. The winter of a given year is defined as starting on October 20 of that year and ending the following March 1. Note the higher average snow depth at Resolute, the station which also had the higher maximum snow depth during most years (unsurprisingly).

3.3 Initialization and Annual Mode Run

As it was mentioned in previous sections, the goal of the annual mode run forced by a skin temperature with the previously discussed definition will be to initialize the sub-surface temperature profile each year in preparation for the full online winter-only, surface balance-driven runs. In the following section, the result of the annual mode simulation is presented, sensitivities to conductive property assumptions are discussed, and a comparison with measurements at Resolute is made.

3.3.1 Annual Mode Results

The result of the annual mode simulation for the time period 1965-2008 is presented in Figure 3.3 for Resolute. Resolute, and this time period in particular, is chosen as the focus for this section because soil measurements are available for the site during a span of 20 years during the 60's to 80's. The figure shows the strong seasonal variation of sub-surface temperatures, which is obviously expected, but also displays the importance of winter snow depth to the deeper temperatures. During the years with little snow (e.g. winters 1966-67, 1976-77, 1984-85), the ground is noticeably colder during the winter.

The quantity of real interest for this study is the winter sub-surface temperature, which is plotted at various depths in Figure 3.4. Notice that the winter temperatures underground are much higher than the air temperature, and continue to increase with depth. This is a result of the time-scale of the temperature change of the soil being smaller than that of the atmosphere. This leads to the deep ground becoming an energy source during the winter, while being an energy sink during the summer, as will be discussed below.

The summer sub-surface temperatures (Figure 3.5) behave in much the opposite way to those of the winter, as would be expected. For one, the temperatures decrease with depth and the air is warmer than the soil. The ground temperatures vary much more like the air temperatures from year to year than in the winters, since there is no insulating snow layer decoupling the two. The summer temperatures also seem to be increasing, which is interesting since this is not the case with the winter temperatures for the same years.

As the temperatures shown above would suggest, the average winter surface conductive flux is upward. Figure 3.6(a) shows this, as a time series for 1965 to 2008. There is variation of up to about 4 Wm^{-2} between years, but the long-term trend seems to be an increasing

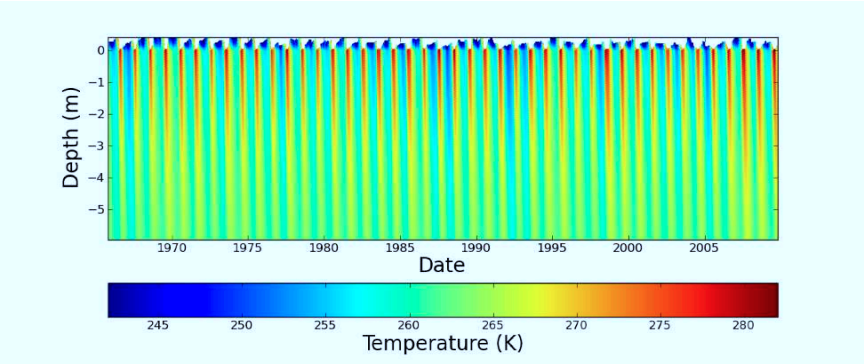

(a) All years

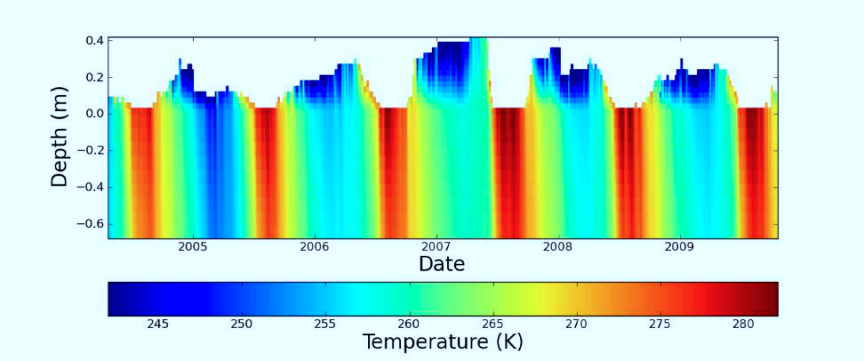

(b) Zoomed in

Figure 3.3: (a) Contour of temperature (K) between the surface and 6 m depth and for the time period Oct 1964 to Mar 2009. This data set was created using the annual mode of the conduction model introduced above. Careful inspection will show that the years of shallowest snow cover tend to be the coldest years for the deeper soil. (b) Zoomed in on shallowest depths and latest years.

one. During the summer, however, the variation is similar but both the flux and the trend go in the opposite direction, as shown in Figure 3.6(b).

Since the direction of the winter and summer fluxes is an obvious result, it is more instructive to examine the annual net flux. This flux, shown in Figure 3.7, is mostly negative, meaning it is an average net flux into the ground from the surface. This should result in annual ground temperatures increasing, as more energy is put into the ground every year during the warm months than is taken out during the cold ones, with the exception of some years such as 1971, 1991, and 1995. These years show unusual behaviour from a combination of smaller snow depths (Figure 3.2(a) and colder summers (Figure 3.5)).

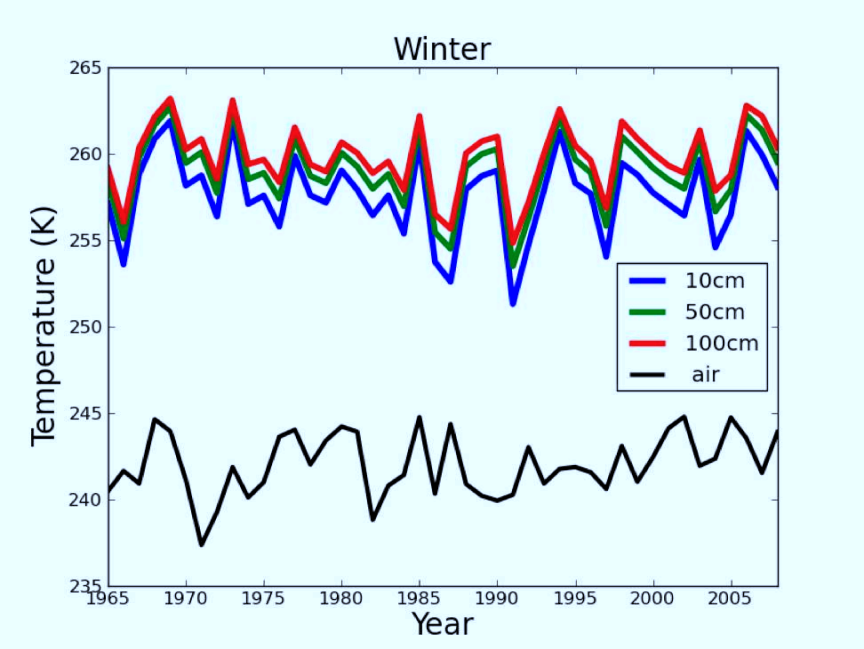

Figure 3.4: Modeled winter average temperature (K) at depths of 10 cm (blue) 50 cm (green) and 1 m (red), as well as air temperature (black). Note the increase in temperature with depth during the winter, which drives the upward heat flux for these months.

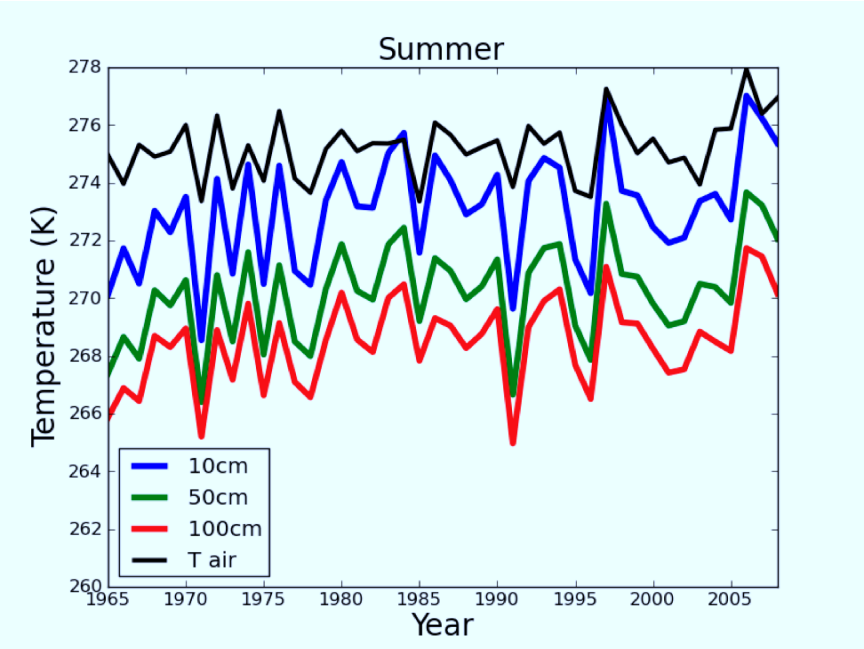

Figure 3.5: The same as Figure 3.4, but for summer (June, July, August). Note the reversal in temperature behaviour, with the deepest layer now being the coldest.

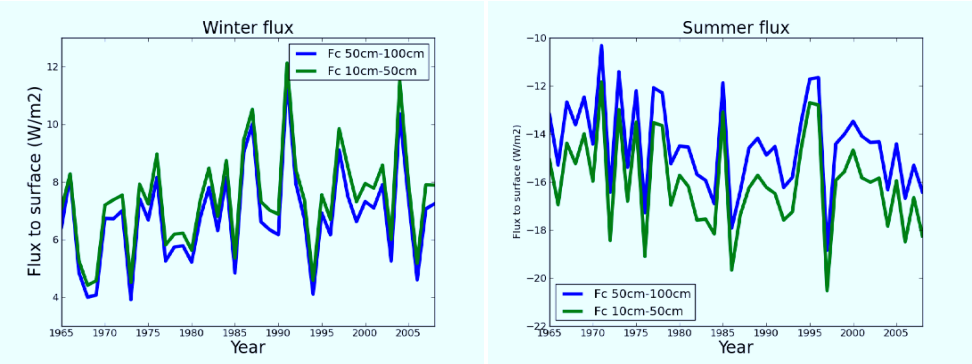

(a) Winter (b) Summer

Figure 3.6: The average a) winter conductive flux and b) summer conductive flux at Resolute between 50 cm and 10 cm depth (green) and 1 m and 50 cm depth (blue), from the annual mode of the conduction model. Positive values are surface-ward. In accordance with the mean temperatures at each depth, the winter values are positive, meaning the ground is supplying the winter surface with energy, while the summer values are strongly negative, as the exposed soil is taking in the abundant radiant energy.

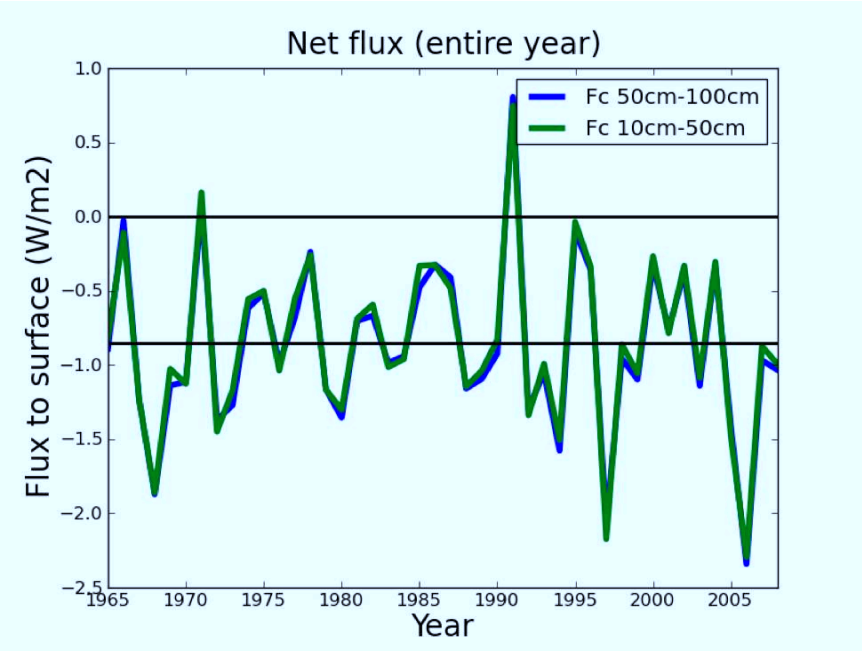

Figure 3.7: Yearly average net flux for Resolute, between the same levels as Figure 3.6(a). The similarity between the two lines indicates that the modeled soil is conserving energy, while the average negative flux indicates that each year (with a couple of exceptions), more energy is being transfered down into the ground during the warm months than is being released during the cold months.

Table 3.2: Snow and soil conductivities for model runs

	k_{snow}=0.15 $Wm^{-1}K^{-1}$	k_{snow}=0.25$Wm^{-1}K^{-1}$	k_{snow}=0.4$Wm^{-1}K^{-1}$
k_{soil} = 2. $Wm^{-1}K^{-1}$		KS3	
k_{soil} = 2.5 $Wm^{-1}K^{-1}$	KS1	default	KS5
k_{soil} = 3. $Wm^{-1}K^{-1}$		KS7	

3.3.2 Sensitivities

Since there were no available measurements of the soil and snow properties at Eureka or Resolute found, there is a large uncertainty in the values chosen for the modeling of the sub-surface conductive flux. To address this issue, sensitivity tests are performed to assess the magnitude of the difference that this forced choice makes. The best estimation is used as a starting point, where the values for the conductivity of snow and soil are chosen to be both likely close to their actual values according to the information available and the literature. This "default" run then becomes the middle ground for the reconstruction, but other runs are performed with more extreme values assumed for the conductive properties, which will give upper and lower bounds to any behaviour displayed in the reconstruction. It should also be noted that neither phase changes in the soil nor movement of water through the active layer are included in this model, and that horizontal transfer of energy into the profile is assumed to be negligible.

Table 3.2 contains the snow conductivity, soil conductivity and name tag of each sensitivity run. The range of snow conductivities comes from the range of possible snow densities, from the less dense (lower conductivity) to the more dense (higher conductivity). The range in soil properties, on the other hand, is due to a range in possible soil types and frozen water contents. Since ice has a relatively high thermal conductivity, the higher the frozen water content of the soil, the higher the thermal conductivity.

Figure 3.8 is a plot of the most important variable, the surface conductive flux, for a collection of sensitivity tests. This is only the flux at a single layer in the conduction model, but is representative of the other layers. The central three lines (purple, blue, red) correspond to the three sensitivity runs performed for varying soil conductivities. The small differences (< 1 Wm^{-2}) between them show that there is little uncertainty due to sensitivity involved with making a reasonable yet incorrect assumption about the soil properties. This

is less true for assumptions about the conductivity of snow, which are reflected in the center and two extreme lines (blue, green, cyan), and carry with them a range of between 14 and 15 Wm^{-2}. This means that the default run annual mode, which is used in the rest of this study, could be biased by 7 to 7.5 Wm^{-2} in either direction, depending on the properties of the snow. The full winter mode sensitivity tests also all show similar behaviour in the diagnosis of the other flux terms. While absolute magnitudes of predicted temperatures and fluxes are dependent on the assumptions made about conductive properties, the character of their evolution in time is not. That is to say, the behaviour of the temperatures and fluxes is universal throughout the sensitivity tests, with the specific values changing by a constant offset from test to test. This behaviour does not take into account the possibility of time-varying conductive properties in the soil and snow, which could further complicate the sensitivity, especially if values of conductive properties and temperature changes are correlated.

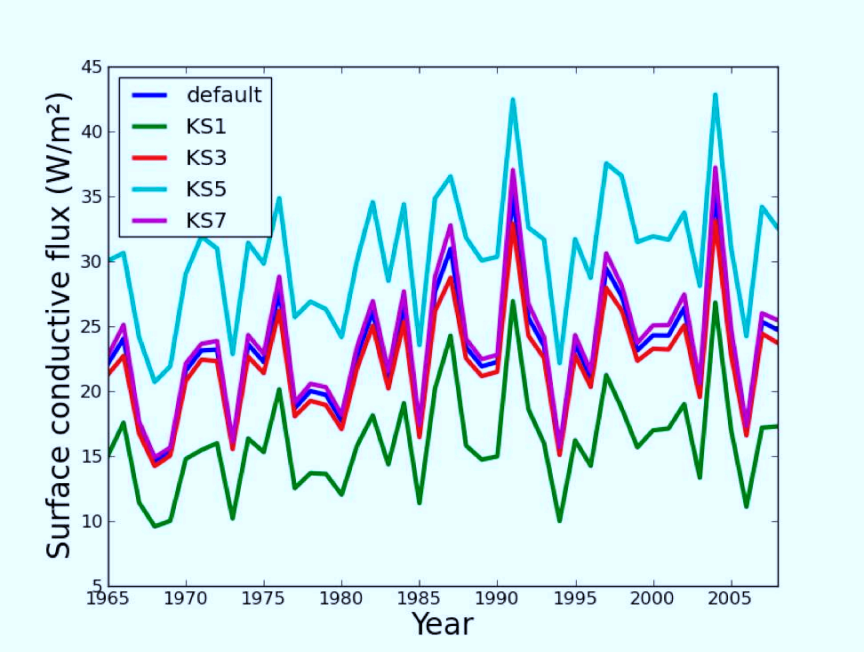

Figure 3.8: Sensitivity test results for winter average surface conductive flux (Wm^{-2}) at Resolute for default (blue), low snow conductivity (green), high snow conductivity (cyan), low soil conductivity (purple) and high soil conductivity (red). Note the stronger conduction dependence on choice of snow conductivity (even compared to the ratio of conductivity ranges used), which creates an uncertainty in flux of up to $\pm$ 7.5 Wm^{-2}. At other depths and for temperature, nearly identical behaviour is observed for these tests.

3.3.3 Comparison to Resolute Measurements

The years 1965 to 1987 were a period when there were soil temperature measurements available in the Environment Canada archive at various depths down to 150 cm at Resolute, which can be used to assess the annual mode's ability to capture the behaviour of the temperature profile. The set of available measurements includes daily averages at 10 cm, 20 cm, 50 cm, 100 cm and 150 cm depths. The data at 10 cm, 50 cm and 100 cm are compared to the same time period and depths from the annual mode of the model (Figure 3.9).

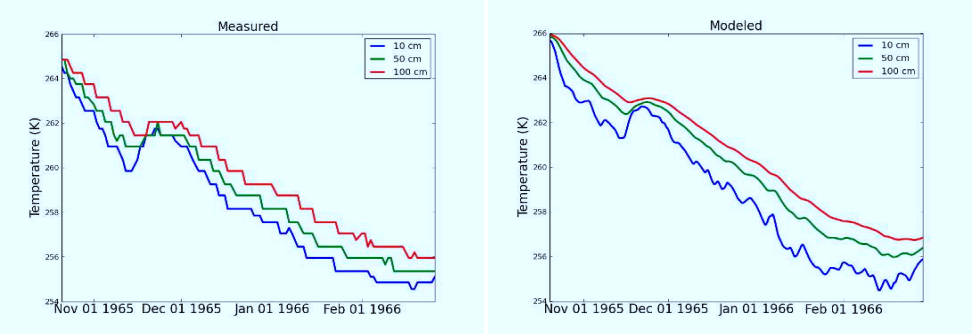

(a) Measured (b) Modeled

Figure 3.9: Time series of measured (a) and modeled (b) temperature (K) between 10 cm depth and 1.5 m depth for the winter 1965-66. The temperature is measured at depths of 10, 20, 50, 100, and 150 cm over the time period.

Figure 3.10(a) and 3.10(b) show the time period of interest for both measured and modeled temperatures, as well as the air temperature, all averaged over the winter months. This comparison shows similar behaviour in the two, and is encouraging, considering the number of simplifications and assumptions involved in the model. The model does, however, have a bias high overall and appears to respond more readily to changes in air temperature, particularly at deeper levels. The measured temperatures at 10 cm and 50 cm show a more decoupled pattern of variation than their modeled counterparts.

As Figure 3.11(a) and 3.11(b) show, the summer in the annual mode is much farther from agreement than the winter. While the pattern of variation is still quite similar, there is a large temperature gradient between 10 and 50 cm in the measurement results which is not nearly as large in the model. This suggests that perhaps there is a layer of insulating material between the two layers at this particular location, but this is merely speculation.

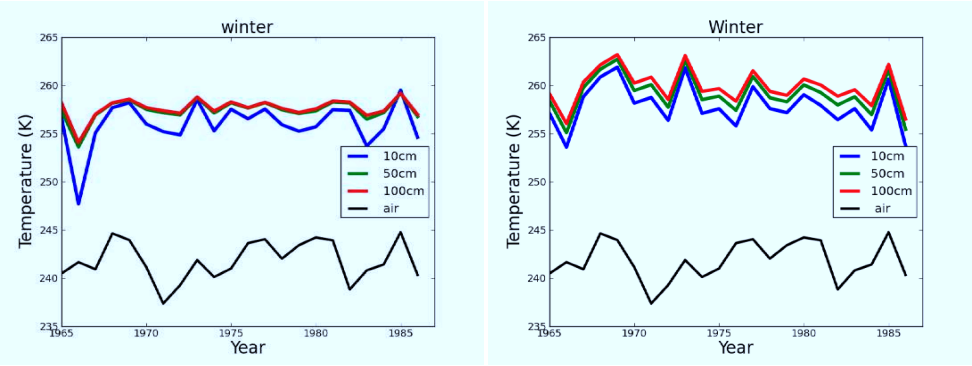

(a) Measured (b) Modeled

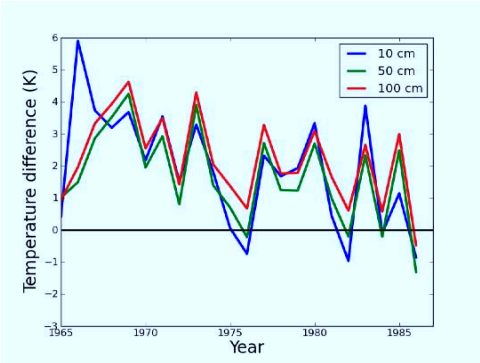

(c) Difference

Figure 3.10: Measured (a) and modeled (b) average winter temperatures (K) at depths of 10 (blue), 50 (green) and 100 cm (red), with measured air temperature in black. The difference between modeled and measured curves is plotted in (c). The measured soil temperatures show a lesser temperature gradient between the deeper two levels.

Another possibility is that there is melting of frozen material occurring in the active layer soil during the summer, which is creating a sink of energy and lessening the flux reaching the deeper layers.

The former hypothesis seems to be more likely when looking at the calculated fluxes in Figure 3.12(a) and 3.12(b). These fluxes were calculated using the assumed soil conductivities used in the model. Since in both summer and winter (and the year overall in Figure 3.13) these differ by a similar factor (~ 5), it would be plausible that the material between these layers has a thermal conductivity about $\frac{1}{5}$ times that of the soil above it. It is, however, possible that this behaviour is due to an unresolved process in the model, such as horizontal heat transfer by moving water or the vertical percolation of water in the active layer and the latent heat it brings with it.

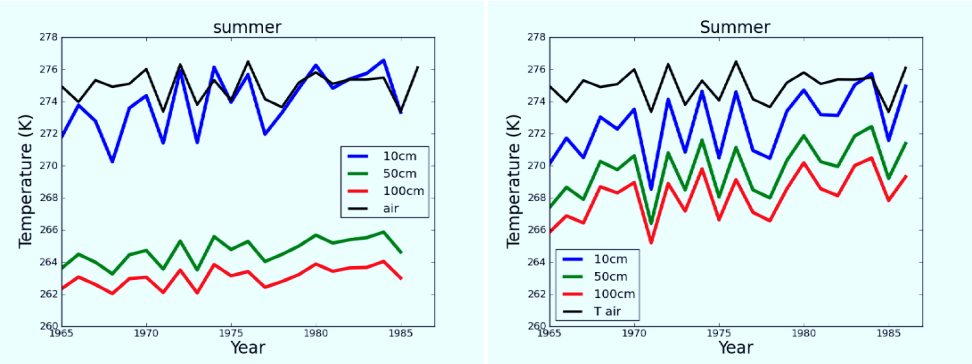

(a) Measured (b) Modeled

Figure 3.11: The same as Figure 3.10, but for summer temperatures. While accurately modeling summer temperatures is not one of the objectives of this study, it is interesting how deviant the modeled temperatures are in the summer. The extremely large temperature gradient between 10 and 50 cm depth in the measurements is potentially due to a layer of some insulating material between those two levels, but speculating on the nature of this layer would be guess-work at best.

While the actual value of the annual net flux, as shown in Figure 3.13 (calculated using the measured temperature values and the assumed soil conductivities), depends on the chosen value of thermal conductivity, the sign, and therefore the direction, does not. In this way, the net flux estimated from measurement shows the same result as that of the model: more energy is going into the ground during the warm months than is being released during the cold months. That is to say, the net flux is from the surface downwards. The value, however, differs from that from the model greatly. This is due to the aforementioned unresolved processes such as latent heat sources and sinks in the active layer, and soil layers differing in conductivity.

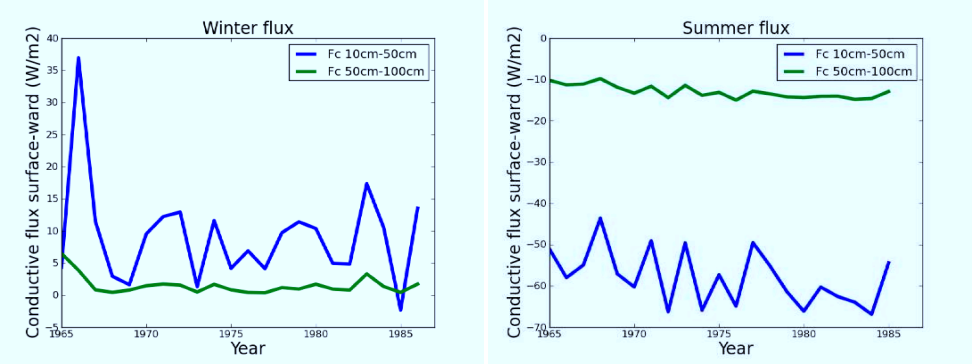

(a) Winter (b) Summer

Figure 3.12: Average winter (a) and summer (b) conductive flux between 50 and 10 cm (blue) and 100 and 50 cm (green), calculated using the measured temperatures at the levels involved and the same assumptions of soil conductivities used in the model. While the directions of these flux results are in agreement with the modeled results, the incredibly large discrepancy between the flux at the two different levels in both summer and winter suggests that there is indeed a material of low conductivity between 10 and 50 cm depth.

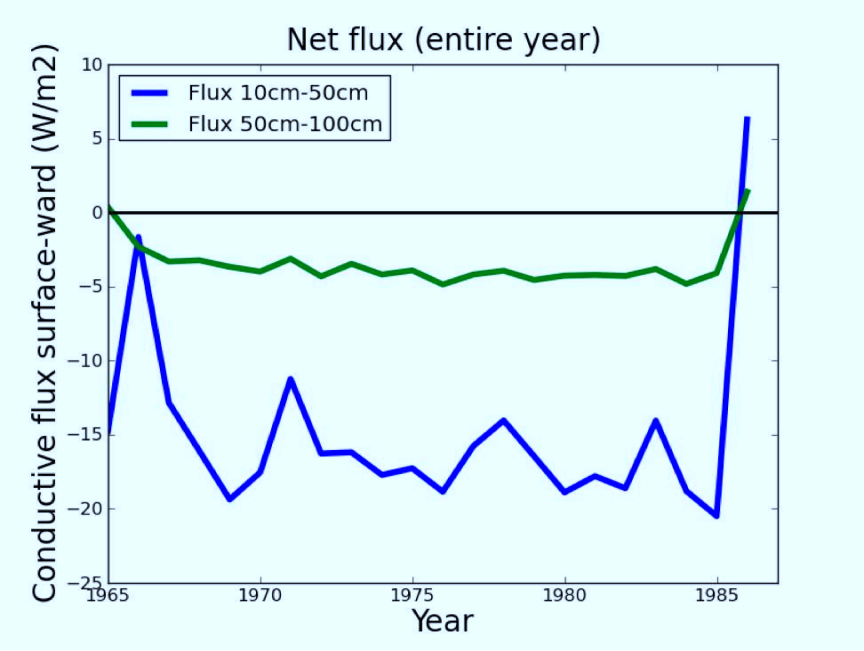

Figure 3.13: Same as Figure 3.12, but whole year averages.

CHAPTER 4

SENSIBLE AND LATENT HEAT FLUX, AND SURFACE ENERGY BALANCE

Previous chapters have discussed the conductive flux from the soil and snow beneath the surface and the radiative effect of the atmosphere above. The final two flux terms of the surface energy balance, which will be discussed below, are also atmospheric terms, but the nature of their energy transfer is much different from that of downwelling irradiance. Sensible heat is transfered when air of different temperatures is mixed by turbulence or diffusion, and in the Arctic winter in the boundary layer is a generally surface-ward flux. Latent heat is transfered with water vapour, which releases stored (latent) energy during its phase changes (mostly deposition in the Arctic winter). Sensible heat flux due to precipitation is ignored.

4.1 Background

In the fully turbulent unstable and neutrally stable boundary layer cases, the most widely accepted method for relating the sensible and latent heat fluxes to temperature and humidity is Monin-Obukhov Similarity Theory (*Monin and Obukhov*, 1954). MOST relates the bulk transfer coefficient for a given conservative quantity (e.g. sensible or latent heat) to empirical functions of dimensionless variables. The dimensionless variables used are ratios of heights of interest with the Monin-Obukhov length, or the "roughness length", which are obtained empirically from observations. The bulk transfer coefficient can then be used

to calculate the sensible and latent heat fluxes between altitude z and the surface by the equations

$$SH = -C_s u(z)\Delta\theta \tag{4.1}$$

$$LH = -C_e u(z)\Delta q \tag{4.2}$$

where C_s and C_e are the bulk transfer coefficients for sensible and latent heat flux, respectively, $u(z)$ is the wind speed at height z and $\Delta\theta$ and Δq are the differences in potential temperature and water vapour mixing ratio between height z and the surface.

Monin-Obukhov Similarity Theory is used for investigation of the stable boundary layer of the Arctic environment by *Grachev et al.* (2007). Using the SHEBA (*Persson et al.*, 2002) data-set, they conclude that in the very stable regime the turbulent transfer of heat is faster than that of momentum, and propose new mathematical forms for the stability functions for Arctic conditions. Pre-dating this study, however, was a simpler scheme to take into account the unaccounted-for energy transfer under stable conditions which was used by *Brown et al.* (2006) to estimate sensible heat flux. This method is based on a "wind-less transfer coefficient" (*Jordan et al.*, 1999), which scales the turbulent flux, even during still periods. An adaptation of these last methods will be used in this work.

4.2 Parametrizations

4.2.1 Sensible Heat Parametrization

The first parametrization of interest is the transfer of sensible heat. The sensible heat flux is calculated from radiosonde information in a manner similar to *Brown et al.* (2006) and *Jordan et al.* (1999), using the equation

$$SH = (\rho_a c_p C_s u + E_0)\frac{d\theta}{dz} \tag{4.3}$$

where ρ_a is the density of air, c_p is the specific heat of moist air, C_s is the sensible heat bulk transfer coefficient, u is the wind speed at 10 m altitude, $\frac{d\theta}{dz}$ is the potential temperature lapse rate calculated from the sounding level closest to the surface, and E_0 is the windless heat transfer coefficient, with an estimated value of 7.7 W m^{-1} K^{-1}. The value used for

C_s is 0.0053 m, which is tuned to give an appropriate average flux of 6 Wm^{-2} on the same order as SHEBA measurements (*Persson et al.*, 2002), and the wind speed and temperature are from radiosoundings. ρ_a is calculated using the formula

$$\rho_a = \frac{100P_a}{R_{gas}(1 + 0.608q)T_a}, \tag{4.4}$$

where P_a (in hPa) and T_a are surface observed pressure and air temperature, respectively, R_{gas} is the gas constant for dry air, and q is the specific humidity (wet air). This calculation is from the ideal gas law for moist air. The final variable from equation 4.3 is c_p, which is calculated (*Wang et al.*, 2010) using

$$c_p = 1004.5(1 + 0.9433q), \tag{4.5}$$

where 0.9433 is the ratio of specific heats at constant pressure of water vapour and dry air.

4.2.2 Latent Heat Parametrization

The final parametrization used in the surface balance equation is similar to *Wang et al.* (2010) and *Jordan et al.* (1999) and is used to calculate the latent heat flux at the surface-atmosphere interface, which takes into account deposition, condensation, and freezing, and the opposing forms of all these processes. It is again a linearization of a non-linear process, and takes the form

$$LH = \rho_a L C_e u \frac{dw}{dz}, \tag{4.6}$$

where ρ_a is the density of air from the previous section, L has a value of 2.83 x 10^6 J kg^{-1} and is the latent heat of vaporization plus fusion, as the surface is below the freezing point throughout most of the winter, C_e is the latent heat flux bulk transfer coefficient, with a value of 0.0013, u is the 10 m wind speed, $\frac{dw}{dz}$ is the water vapour mixing ratio gradient between the air at the first sounding level above the surface and the mixing ratio at the surface itself. Similarly to *Jordan et al.* (1999), no windless transfer coefficient is used for latent heat, as it was found to have no significant effect over snow surfaces. The difference between the sensible and latent heat parametrizations for the current work and those in the literature mentioned above is the use of the lapse rate of temperature and water vapour in the atmosphere for the former, rather than the difference between the 2 m and skin levels

for the latter.

4.2.3 Sensible Heat Reconstruction

The winter average sensible heat fluxes calculated from radiosondes, for both Eureka and Resolute, are shown in Figure 4.1. The average winter energy transport by sensible heat is positive (surface-ward), which is due to the warmer air being aloft in the Arctic atmospheric inversion. Neither shows a significant trend in its behaviour. Resolute's sensible heat flux is higher, on average, than Eureka's and is more variable from winter to winter.

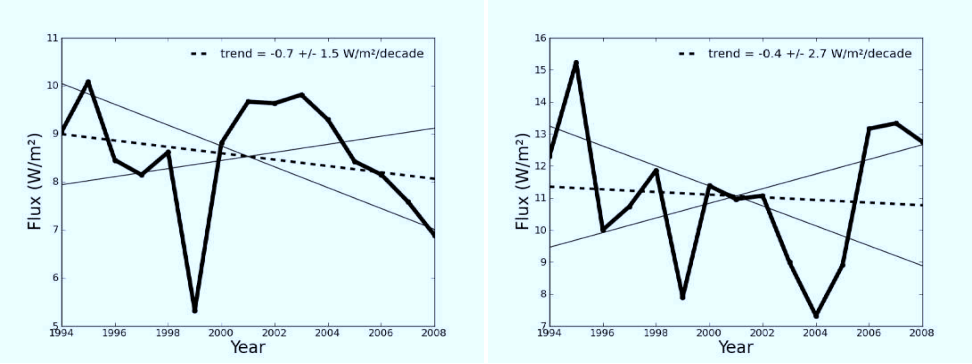

(a) Eureka (b) Resolute

Figure 4.1: Winter average sensible heat flux to the surface for Eureka (a) and Resolute (b). The linear fit of Eureka's sensible heat has a slope of -0.7 $\pm$ 1.5 $\mathrm{Wm^{-2}decade^{-1}}$, while that of Resolute is -0.4 $\pm$ 2.7 $\mathrm{Wm^{-2}decade^{-1}}$.

4.2.4 Latent Heat Reconstruction

The latent heat flux in both locations, shown in Figure 4.2, has the lowest magnitude of all the surface fluxes, particularly at Eureka, where it is almost negligible. At both locations, the latent heat flux, is showing a slightly decreasing trend, but with no statistical certitude. Like the sensible heat reconstruction, the latent heat is of the same order of magnitude as the SHEBA measurement results.

4.3 Surface Energy Balance

The behaviour of the surface climate is ultimately determined by the surface energy balance, which is a frame-work used to simplify and understand the transfer of energy at the

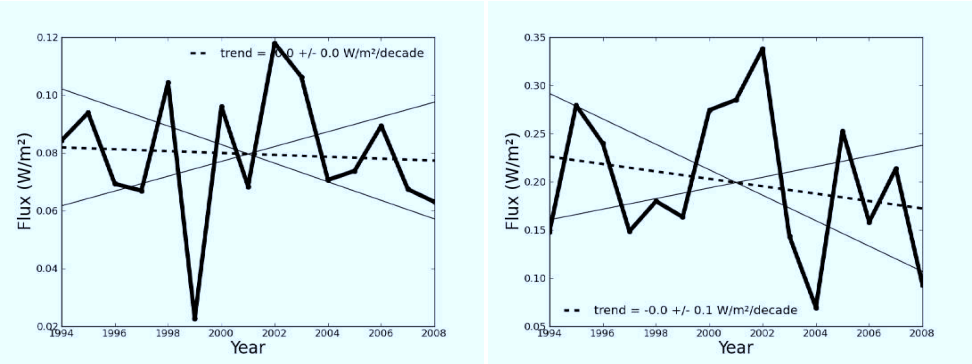

(a) Eureka (b) Resolute

Figure 4.2: Winter average latent heat flux for Eureka (a) and Resolute (b). The linear fit of Eureka's latent heat has a slope of 0.00 $\pm$ 0.01 $Wm^{-2}decade^{-1}$, while that of Resolute is -0.03 $\pm$ 0.04 $Wm^{-2}decade^{-1}$.

ground-atmosphere interface. The surface balance is made up of many components, which cover the range of possible ways energy can be transported from one medium to another, or from one form to another. It relies on the law of conservation of energy, and it describes the behaviour at an infinitesimal layer (skin) at the interface of atmosphere and, in the Arctic case, snow. The goal of balancing the surface energy budget is to be able to diagnose where and how energy passes through the surface skin, and thereby gain insight into the factors and causes of the changing Arctic climate.

4.3.1 Background

Foken (2008) describes the surface balance closure problem and its difficulties in a review of more than 20 plus years of research on the subject. A common problem with surface budget measurement studies is an imbalance resulting from an underestimation of the turbulent fluxes, the sensible and latent heat fluxes.

Studies of the surface energy balance itself have been performed for Arctic environments before; for example *Persson et al.* (2002) discussed the balance in the context of the suite of measurements made during the SHEBA campaign. They report atmospheric cooling by sensible heat flux during the winter, and large variation in the surface budget over relatively short time-scales. The SHEBA study also found that energy from their surface budget was going into the loss of snow and ice causing an imbalance in the measured fluxes, but an imbalance that was consistent with the measured phase changes.

Ling and Zhang (2004) use the surface energy balance to drive a permafrost conduction model, by allowing a varying snow layer, the top of which is defined as the surface. Ling and Zhang report success in their ability to recreate the temperature profile in many layers of the permafrost at Barrow, but point out that unknown snow density can have a large effect on results of such a study.

Wang et al. (2010) also use surface energy balance as a driver for a model, theirs being an ice thickness model to be used with satellite remote sensing. Although their estimations of downwelling longwave irradiance and sensible heat are cruder than those used for this work, they report success in estimation of ice thickness when compared to in situ measurements, at least in dark sky cases without the complicating solar irradiance.

4.3.2 Surface Balance

The equation of surface energy balance for the Arctic winter is a simplified version of

$$SW_{down} - SW_{up} + LW_{down} - LW_{up} + SH + LH + C = 0 \tag{4.7}$$

where SW is the short-wave flux, LW is the long-wave flux, SH is the sensible heat, LH is the latent heat, and C is the conductive flux, and the effect of water soaking into the soil (and bringing with it latent heat) is neglected. Positive terms in this formulation indicate surface-ward flux. The simplification can occur thanks to lack of insolation that the High Arctic experiences for up to four months of each year. The sun going down below the southern horizon for months at a time creates a surface where the fluxes of incoming and outgoing short-wave radiation can be comfortably neglected, leaving the radiative forcing to the long-wave part of the spectrum alone.

$$SW_{down} = SW_{up} = 0 \tag{4.8}$$

Along with the positive (surface-ward) radiation forcing from the atmosphere (Chapter 2) and the positive conductive contribution from the ground (Chapter 3), the surface at dark winter sites such as Eureka and Resolute experiences the effects of other fluxes that are unidirectional for the season of interest. The first of these, the upwelling long-wave radiation (Chapter 1), is by definition unidirectional in the surface balance, as it is always an upward flux. This is the black-body radiation given off by an object at the temperature of

the surface skin. The second flux is the sensible heat flux (Chapter 4), which is the surfaceward (for the most part) transfer of energy from the atmosphere due to turbulent eddies which bring warmer air in contact with the colder surface, and is somewhat dependent on the wind as a driver. Finally, the flux of the smallest magnitude is the latent heat flux (Chapter 4), which is the result of air of different humidity being mixed toward the surface, releasing energy through condensation and deposition.

These fluxes come together at the atmosphere-snow interface to determine the surface energy budget. Solving the energy balance equation is a matter of finding the skin temperature T_s for which the sum of the flux terms is zero, which is done numerically at each time-step using the pre-computed sensible, latent, and radiant downwelling fluxes, and the sub-surface temperature profile. The total equation for surface balance in this form is

$$DW - \epsilon\sigma T_s^4 + SH + LH - k_{snow}\frac{T_s - T_g}{\Delta z} = 0 \tag{4.9}$$

where DW, SH, and LH are the prescribed downwelling irradiance, sensible heat flux and latent heat flux, ϵ is the surface emissivity, σ is the Stefan-Boltzman constant, k_{snow} is the thermal conductivity of snow, T_s is the skin temperature, T_g is the ground temperature in the layer below the surface skin and Δz is the thickness between skin and ground layers. Since the value of skin temperature determines the amount of conductive flux to the surface, which in turn determines the progression of the temperature profile, the conduction model discussed in Chapter 3 must be run simultaneously with the surface balance solver. This procedure is shown in the flowchart Figure 4.3.

4.3.3 Winter Surface Flux Reconstruction

Presented below are the results of the winter surface balance model, for the time period 1994-95 to 2008-09. The model was run using the downwelling irradiance (Chapter 4, Section 2), and sensible and latent heat fluxes (Chapter 4) as forcings at every hourly timestep. The resulting predicted upwelling irradiance and conductive flux are shown below, along with the total energy budget each year for the modeled time period.

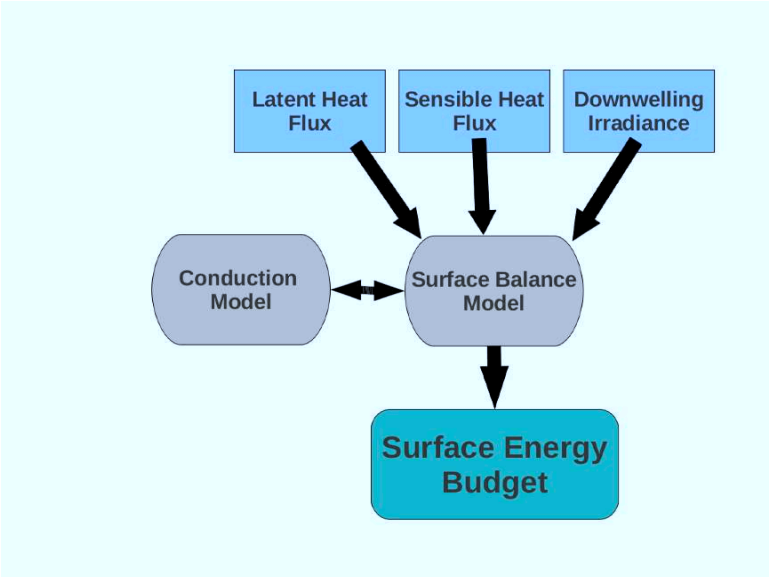

Figure 4.3: Flowchart of model layout. The calculated downwelling irradiance, sensible heat flux, and latent heat flux are inputs for the surface balance model which is coupled with the conduction model to produce the surface energy budget.

4.3.3.1 Radiation

During Eureka's winters since 1994, the predicted downwelling irradiance has been on the rise, as shown in Chapter 2 and Figure 4.4(a). This rise is reflected in the opposing upwelling radiation, which also has an upward trend, as shown in Figure 4.4(b). The trend is significant, as the 95 percent confidence interval for slopes shows, but is not as large as that of its downwelling counterpart. This leads to increasing net radiation (where net radiation is the total downward irradiance minus the total upward irradiance), as shown in Figure 4.6(a), although the slope of the net radiation trend has an uncertainty large enough that it is possibly not increasing.

A similar situation presents itself at Resolute, where both the downwelling (Figure 4.5(a)) and upwelling (Figure 4.5(b)) irradiances show large increases that are statistically significant. Unlike at Eureka, these increases are happening at closer to the same rate, and with lower relative uncertainties. This means that once again unlike Eureka, it would be difficult to argue any change in the net radiation at the surface, due to the statistical insignificance of any calculated trend in this quantity. The net radiation for Resolute is shown in Figure 4.6(b).

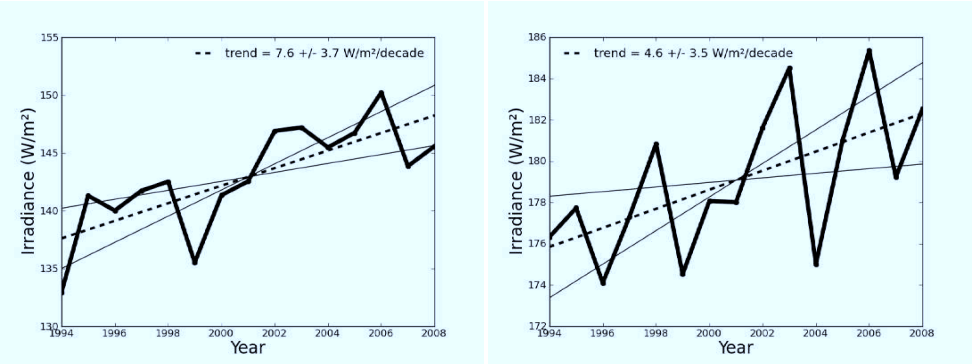

(a) Downwelling (b) Upwelling

Figure 4.4: Winter average reconstructed downwelling (a) and upwelling (b) radiation for Eureka. The linear fit of downwelling radiation has a slope of 7.6 $\pm$ 3.7 $\mathrm{Wm^{-2}decade^{-1}}$, while that of upwelling radiation is 4.6 $\pm$ 4.5 $\mathrm{Wm^{-2}decade^{-1}}$.

4.3.3.2 Conductive Flux

The winter average conductive fluxes for Eureka and Resolute are shown in Figures 4.7(a) and 4.7(b) respectively. In both cases the flux is strongly surface-ward, a result of the sub-surface temperatures being warmer than the air and surface during the winter (see Chapter 3). At Eureka, there is possibly a downward trend in conductive flux at the surface over the time period, but it is a relatively uncertain one, as the 95 percent confidence interval includes positive slopes. At Resolute, however, there is essentially no signature of a trend whatsoever.

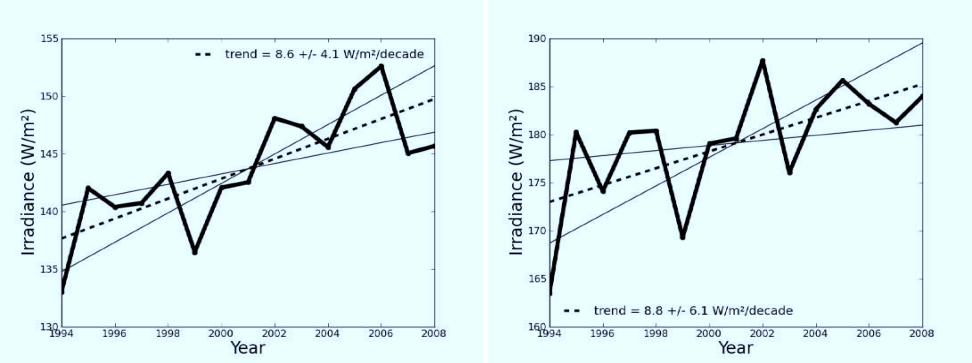

(a) Downwelling (b) Upwelling

Figure 4.5: Winter average reconstructed downwelling (a) and upwelling (b) radiation for Resolute. The linear fit of downwelling radiation has a slope of 8.6 $\pm$ 4.1 $Wm^{-2}decade^{-1}$, while that of upwelling radiation is 8.8 $\pm$ 6.1 $Wm^{-2}decade^{-1}$.

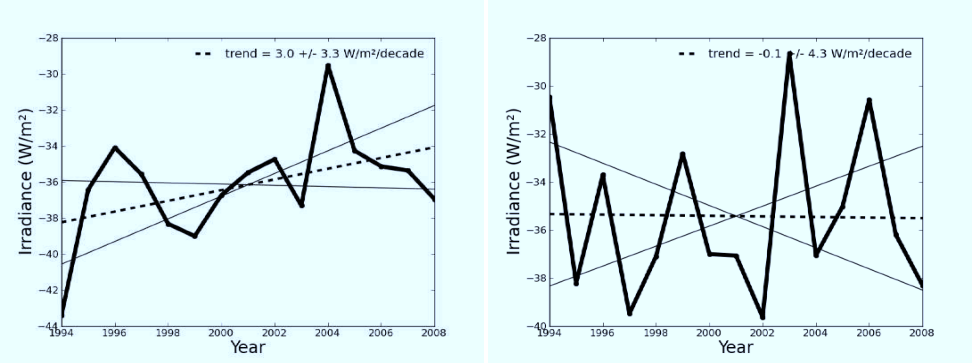

(a) Eureka (b) Resolute

Figure 4.6: Winter average net radiation for Eureka (a) and Resolute (b). The net radiation is the radiation towards the surface minus the radiation away from the surface (i.e. downwelling - upwelling). The linear fit of Eureka's net radiation has a slope of 3.0 $\pm$ 3.3 $Wm^{-2}decade^{-1}$, while that of Resolute is -0.1 $\pm$ 4.3 $Wm^{-2}decade^{-1}$.

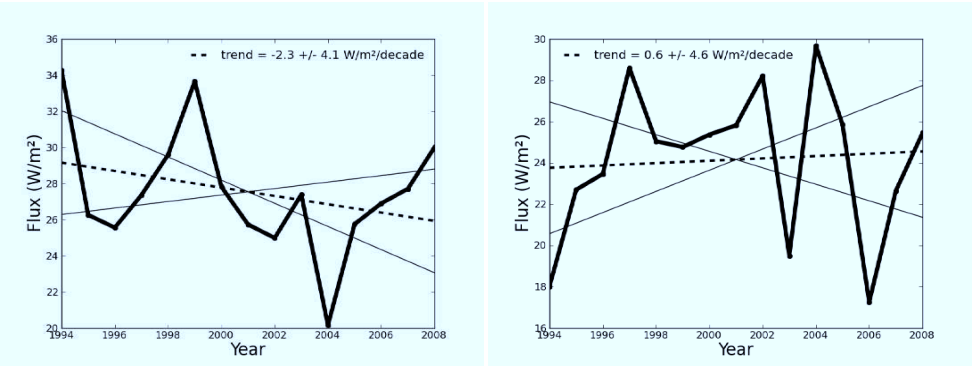

(a) Eureka (b) Resolute

Figure 4.7: Winter average conductive flux for Eureka (a) and Resolute (b). The linear fit of Eureka's conductive flux has a slope of -2.3 $\pm$ 4.1 $\mathrm{Wm^{-2}decade^{-1}}$, while that of Resolute is 0.6 $\pm$ 4.6 $\mathrm{Wm^{-2}decade^{-1}}$.

4.3.3.3 Total Budget

With a reconstruction of all of the terms of the surface energy balance, the total energy budget for each winter can be calculated. The average total energy transfered to the surface during the winter of each year is the sum of all the surface-ward fluxes: the downwelling irradiance, the conductive flux, and the surface and latent heat fluxes which are summed together for simplicity. Figure 4.8(a) is a graph representing the total surface-ward flux for each year as well as the fraction of this total that is contributed by each of the aforementioned fluxes for Eureka. There is little fractional variation winter-to-winter, with the downwelling irradiance always dominating and the conductive flux contributing more than the sensible plus latent heat every year. The same is true for Resolute (Figure 4.8(b)), although there is more variability year-to-year in the total budget for the more southern station.

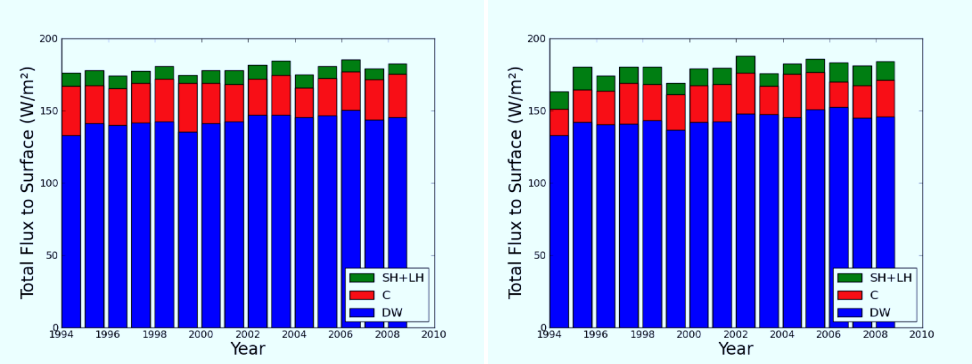

(a) Eureka (b) Resolute

Figure 4.8: Total flux of energy to the surface during the winter for Eureka (a) and Resolute (b). The blue represents the downwelling irradiance, the red the conductive flux and the green the sensible and latent heat fluxes. The combined height of each bar is the total energy flux to the surface for that year.

CHAPTER 5

ANALYSIS AND DISCUSSION

During the course of the previous three chapters, winter reconstructions were put forward for downwelling long-wave irradiance, sub-surface conduction and temperature changes, and relevant surface fluxes. In the following chapter, these reconstructions will be discussed, along with the causes of the time-varying behaviour, with the goal of gaining understanding of the causes behind the increasing surface air temperature, plotted in Figure 5.1.

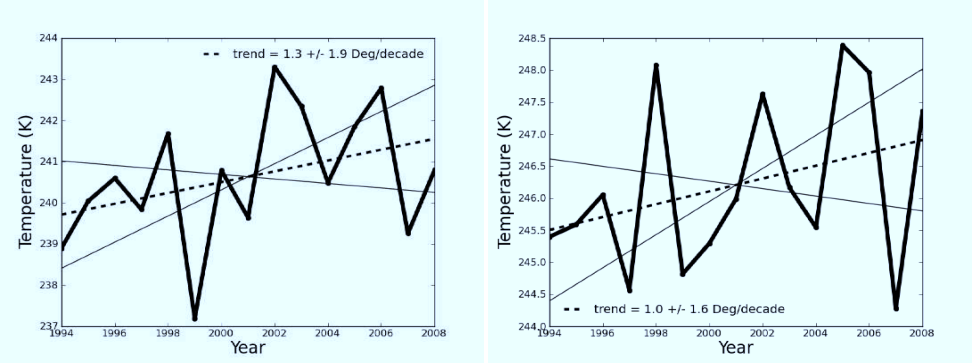

(a) Eureka (b) Resolute

Figure 5.1: Winter average surface air temperature for (a) Eureka and (b) Resolute.

5.1 Downwelling Radiation

The downwelling radiation reconstructions for both Eureka and Resolute show a similar behaviour, but on different scales. During the time period of the winters 1994-2008, the

downwelling irradiance was very strongly increasing. The significance of this increase and its causes are discussed below in two sections, one for Eureka and a second for Resolute.

5.1.1 Eureka

Eureka's reconstructed downwelling irradiance is repeated in Figure 5.2. The marked increase over the examined time period is a significant one, with a trend of 7.9 Wm^{-2} per decade and an uncertainty in the slope of 3.7 Wm^{-2}. The largest deviations from the warming trend come in the winters 1999-00 and 2007-08. During the winter 1999-00, there is an 8 Wm^{-2} decrease in irradiance from the previous year, but afterwards the irradiance continues on as it was, increasing linearly. The cause of the increasing trend in general must be either the behaviour of the temperature and water vapour signals which make up the clear-sky irradiance or the cloud forcing or a combination of the two.

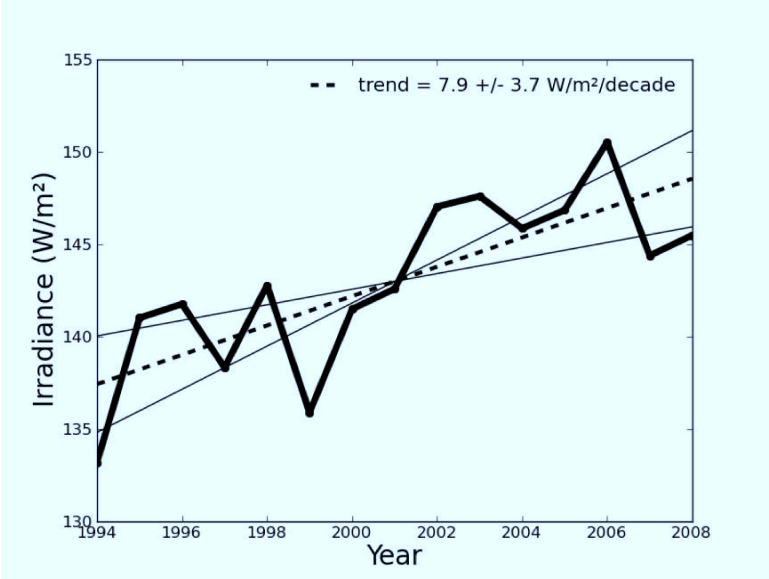

Figure 5.2: Winter average reconstructed downwelling radiation for Eureka. The linear fit of the downwelling irradiance has a slope of 7.9 $\pm$ 3.7 $Wm^{-2}decade^{-1}$. Same as Figure 2.10

To begin, Figure 5.3 shows the clear-sky irradiance for Eureka for the time period of interest, where "clear sky" irradiance is the calculated irradiance with clouds excluded from the model. By removing the clouds, the behaviour is simplified to be that caused by the changing water vapour and temperature profiles that affect the cloudless downwelling

irradiance directly. The clear sky irradiance shows a higher fractional variability inter-annually, and a less steep increasing trend, at 3.5 Wm^{-2} per decade with an uncertainty in the slope of 3.4 Wm^{-2} per decade. The interesting 1999-00 winter which showed a considerable drop in the overall irradiance is also the minimum year for clear sky irradiance in the reconstructed time-period. 2007-08 is also a minimum locally for clear skies.

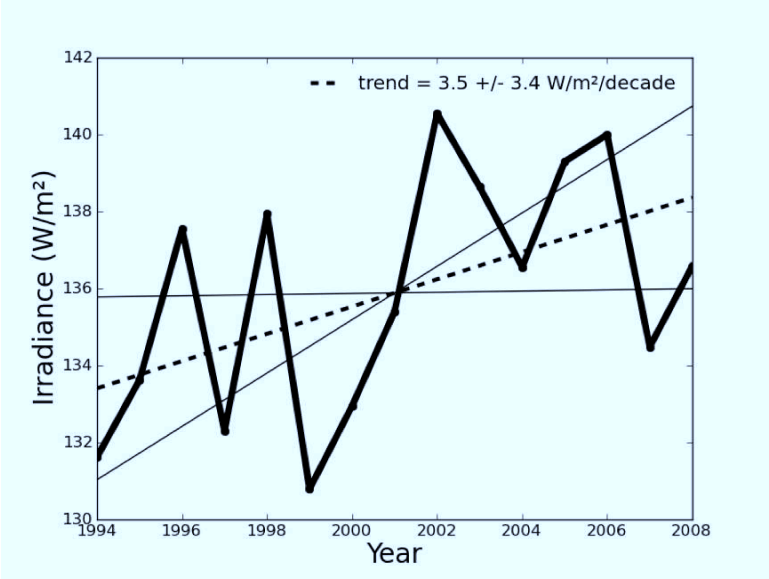

Figure 5.3: Winter average reconstructed clear sky downwelling radiation for Eureka. The linear fit of the downwelling irradiance has a slope of 3.5 $\pm$ 3.4 $Wm^{-2}decade^{-1}$. The clear sky irradiance is calculated by re-running the SBDART code with clouds removed.

To properly diagnose a cause for the variability and trend in the clear sky signal, two factors are the atmospheric temperature aloft and the column precipitable water. The first of these is shown in Figure 5.4, which shows the average winterly temperature at the 700 mb pressure level for Eureka. While the 700 mb temperature is not the only important temperature determining the downwelling flux, its behaviour is indicative of the similar behaviour of the 850 mb and 500 mb temperatures as well. The temperature shows a rising trend of 0.7 degrees per decade, but with an uncertainty larger than that (1.0 degrees per decade).

The other factor of interest for explaining the increase in clear sky irradiance is the water vapour content of the atmosphere. Figure 5.5 shows the winter average integrated water vapour profile up to 5 km during the time period of interest. Much like the atmospheric temperature, the integrated water vapour is showing a trend of increase, finishing at a value

about 10% higher than it started at, but the uncertainty in the slope indicates that we cannot have 95 percent confidence that there is a real trend displayed in these data. With both the integrated water vapour and temperatures displaying a lack of convincing increasing trends, it is important to point out that it is not simply the average of these values that determines the downwelling irradiance, but a somewhat correlated interaction between when the temperature is high, and in what part of the lower troposphere the water vapour resides in.

With the temperature and water vapour content each possibly increasing over the time period, it would be reasonable to say that their enhancements are each contributing to the increased irradiance, but their relative contributions are not clear. To quantify the contribution from each of these changing properties, and to capture the effect on the irradiance of each, two model runs are performed: one using a 1994-2008 winter average water vapour profile and the actual varying temperature profiles for each sounding, and the other using 1994-2008 winter averaged temperature profile and the actual varying sounding water vapour profiles. The change of irradiance from year to year in these simulations will be the contribution of changing temperature and water vapour in the atmosphere, respectively.

Figure 5.6(a) shows the effect of the changing atmospheric temperature. The values shown in the figure are the changes with respect to the first year (1994-95) in the winter average irradiance. The temperature effect shows an increasing trend (2.1 Wm^{-2} per decade), but multiple negative years and a larger uncertainty than slope. So while the temperature's long-term effect on the irradiance is possibly an enhancement, the inter-annual variability of this signal is large.

Figure 5.6(b) shows the second simulation, which assesses the contribution of changing water vapour to the overall change in downwelling irradiance. This signal is less strong in terms of magnitude of increase, with a trend of 1.7 Wm^{-2} per decade, but is showing less relative inter-annual variability than its temperature counterpart. The low uncertainty of 1.0 Wm^{-2} per decade means that the water vapour's behaviour has less inter-annual variability than temperature.

The combination of these two effects makes up the overall changing irradiance, and to show this, Figure 5.7 shows a comparison of the overall change in clear sky irradiance (change since 1994-95) to the sum of the temperature and water vapour effects. The two lines are essentially identical, and this closure lends validity to the method of decomposing

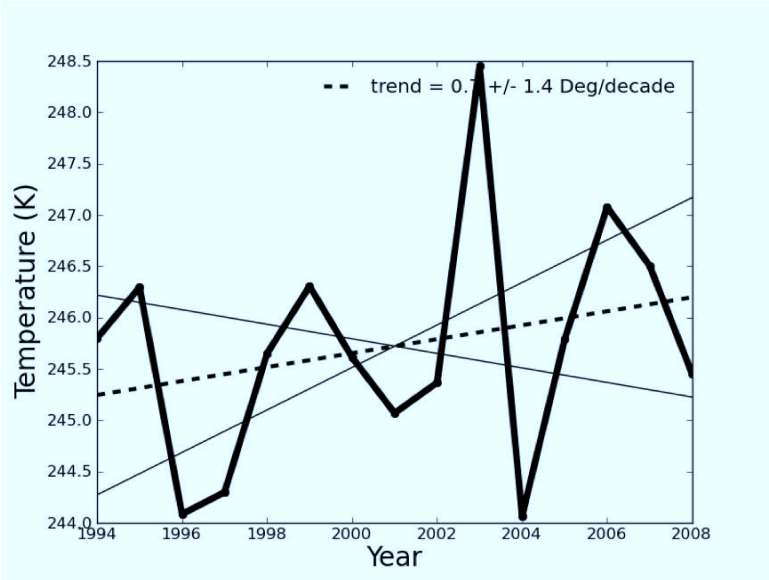

Figure 5.4: Temperature time-series at the 700 hPa level at Eureka. Values are averages over the whole winter, and the linear fit has a slope of 0.7 ± 1.4 K decade^{-1}. The 850 hPa (0.3 ± 1.5 K decade^{-1}) and 500 hPa (0.6 ± 1.4 K decade^{-1}) levels behave in much the same way.

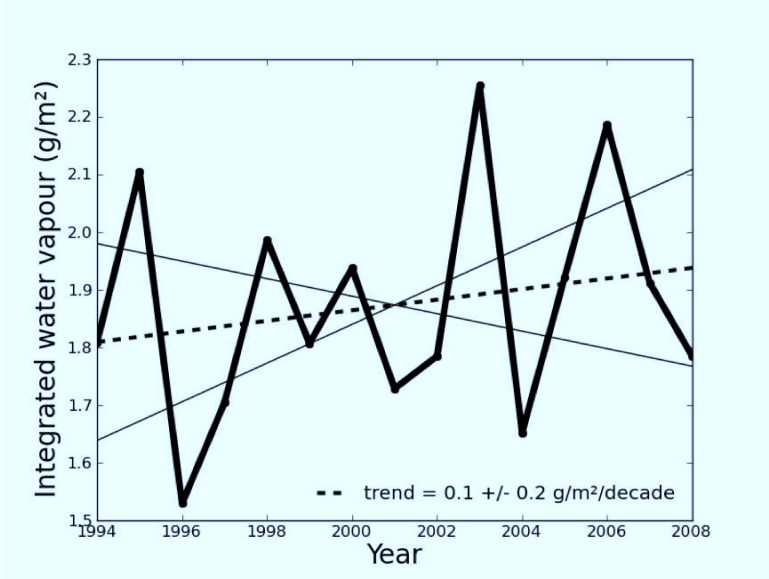

Figure 5.5: Integrated water vapour time-series at Eureka. Values are averages over the whole winter, and the linear fit has a slope of 0.1 ± 0.2 g m^{-2} decade^{-1}.

Table 5.1: Summary of irradiance contributions at Eureka

Effect	Contribution per decade
Cloud	4.4 Wm^{-2}
Clear (Water vapour/Temperature)	3.5 (1.7/2.1) Wm^{-2}
Total	7.9 Wm^{-2}

the water vapour and temperature effects into separable quantities. This result matches the one from the 3 day case study of *Doyle et al.* (2011) discussed in Chapter 2.

Much as the clear sky irradiance increased over the time period studied, so too did the clouded sky irradiance. This is plotted in Figure 5.8, and was calculated by subtracting the clear sky downwelling irradiance from the total downwelling irradiance. The cloud forcing shows an increase of 4.4 $\pm$ 1.8 Wm^{-2} per decade, and less variability around this trend than was seen in the temperature, water vapour, and total clear sky fields. Since the cloudiness in this simulation is based on a relative humidity threshold (see section 2.2.3.1), this upward trend should be caused by an increase in relative humidity.

Figure 5.9(a) displays the trend in relative humidity, which is positive overall, but highly uncertain with a slope of 2.1 %/decade but a 95 percent confidence interval 3.9 %/decade higher and lower than this. The relative humidity plotted here is an average relative humidity for the lower troposphere (5 km altitude and lower), and shows a surprisingly large increase over the mid-late 90s and into the mid 00s of around 8 %. This increase comes with a likely upward trend in days with cloud (Figure 5.11), but likely does not correspond to an increase in surface observed cloud fraction (Figure 5.10).

Table 5.1 summarizes the contributions to increasing irradiance at Eureka. Note that the fact that the water vapour effect and temperature effect trends do not sum to the clear trend is a reflection of the imperfect match between the two lines of Figure 5.7.

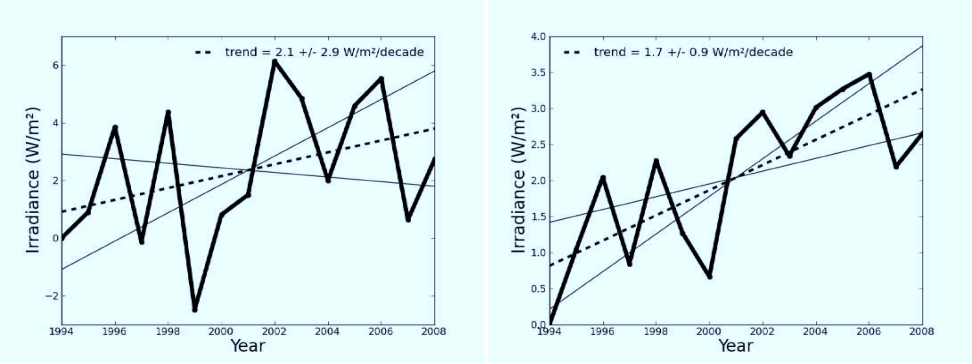

(a) Temperature's effect (b) Water vapour's effect

Figure 5.6: (a) Temperature's effect on irradiance for Eureka. The linear fit of the temperature effect has a slope of 2.1 $\pm$ 2.9 $Wm^{-2}decade^{-1}$. This is the change in irradiance since the starting winter due to changing temperature. To calculate this value, the SBDART code was run with a constant water vapour profile (the all-radiosonde winter mean) while allowing the temperature to vary. (b) WV's effect on irradiance for Eureka Water vapour's effect on irradiance for Eureka. The linear fit of the water vapour effect has a slope of 1.7 $\pm$ 0.9 $Wm^{-2}decade^{-1}$. This is the change in irradiance since the starting winter due to changing water vapour. To calculate this value, the SBDART code was run with a constant temperature profile (the all-radiosonde winter mean) while allowing the water vapour to vary.

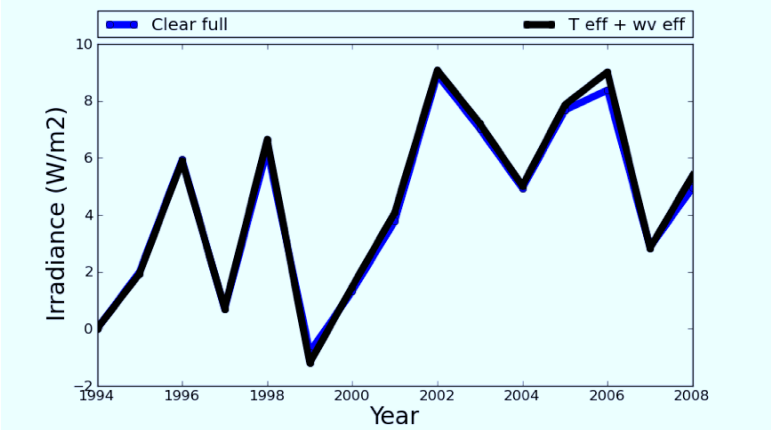

Figure 5.7: Closure of temperature and water vapour effects on irradiance for Eureka. The blue line is the change in irradiance since 1994 in the full clear sky simulation (water vapour and temperature varying), and the black line is the sum of the water vapour and temperature effects shown in Figures 5.6(b) and 5.6(a) respectively.

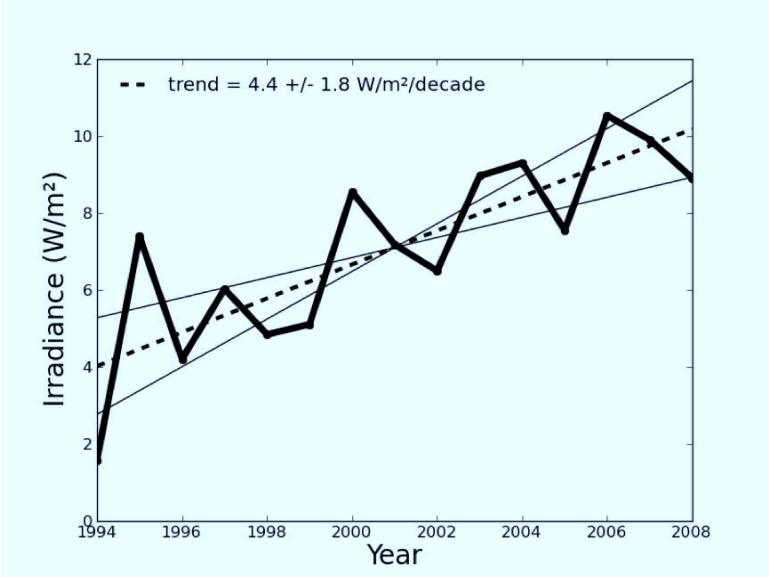

Figure 5.8: Winter averaged reconstruction of the effect of clouds on irradiance at Eureka. The linear fit of the cloud effect has a slope of 4.4 $\pm$ 1.8 $\mathrm{Wm^{-2}decade^{-1}}$. The cloud effect is calculated by subtracting the clear sky irradiance from the full simulated irradiance.

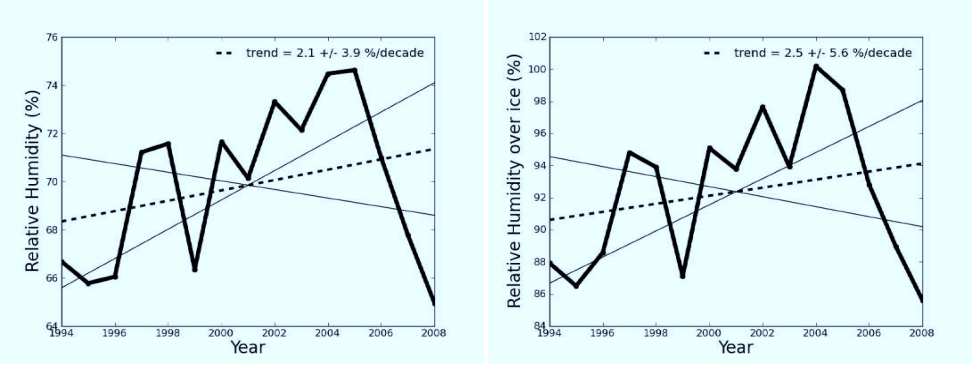

(a) RH (b) RHice

Figure 5.9: Lower-troposphere (average from surface to 5 km) relative humidity with respect to water (a) and with respect to ice (b) time-series at Eureka from radiosondes. Values are averages over the whole winter, and the linear fit has a slope of 2.1 $\pm$ 3.9 % $\mathrm{decade^{-1}}$ for RH_{water} and 2.5 $\pm$ 5.6 % $\mathrm{decade^{-1}}$ for RH_{ice}. The lower-troposphere relative humidities are an average of the relative humidity from the surface to 5 km.

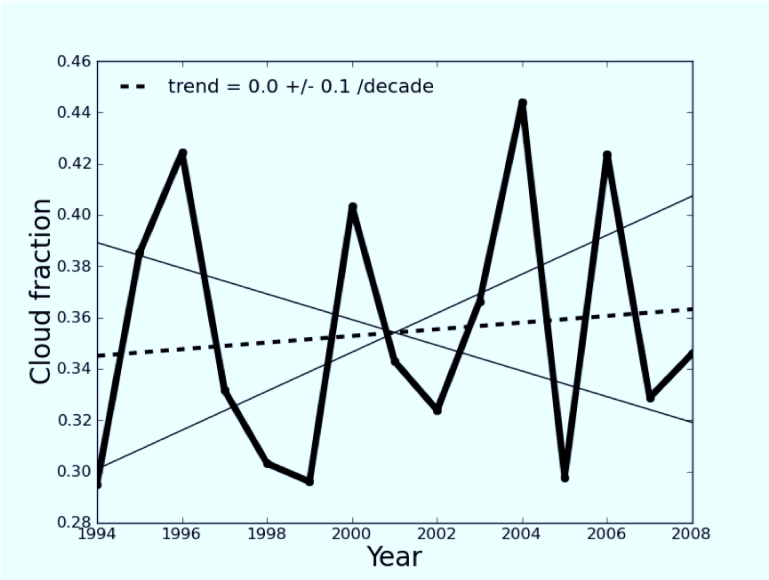

Figure 5.10: Surface observed cloud fraction time-series at Eureka. Values are averages over the whole winter, and the linear fit has a slope of 0.0 ± 0.1 decade^{-1}.

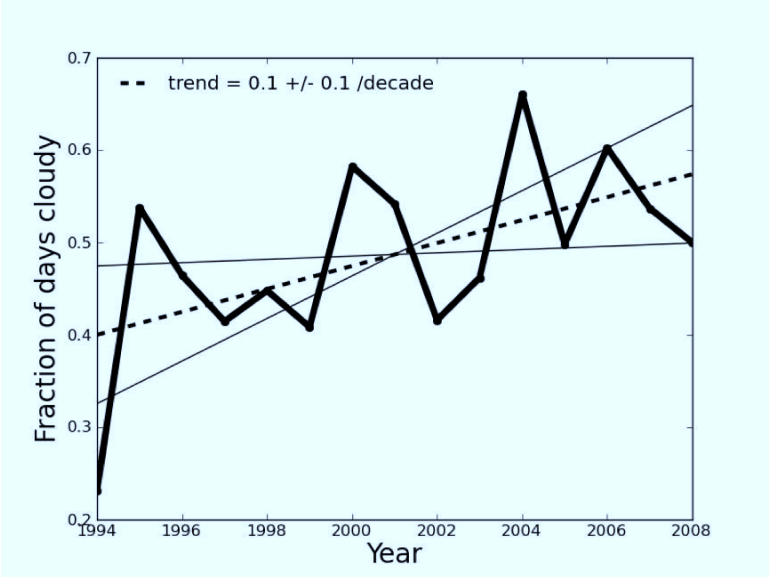

Figure 5.11: Radiosonde method fraction of times with cloud time-series at Eureka. Values are averages over the whole winter, and the linear fit has a slope of 0.1 ± 0.1 decade^{-1}. The fraction of days with cloud is the ratio of the number of times that the reconstruction included a cloud and the total number of time points.

5.1.2 Resolute

Like Eureka, Resolute had an increasing trend in downwelling radiation over the 1994-2009 time period. Figure 5.12 shows this trend to be a strong one, at 14.8 $\pm$ 6.7 Wm^{-2} per decade. Unlike Eureka, however, there is not a strong increasing signal in the clear sky irradiance (although the trend from regression is a positive one, the uncertainty is substantially larger than the slope). This is reproduced in Figure 5.13.

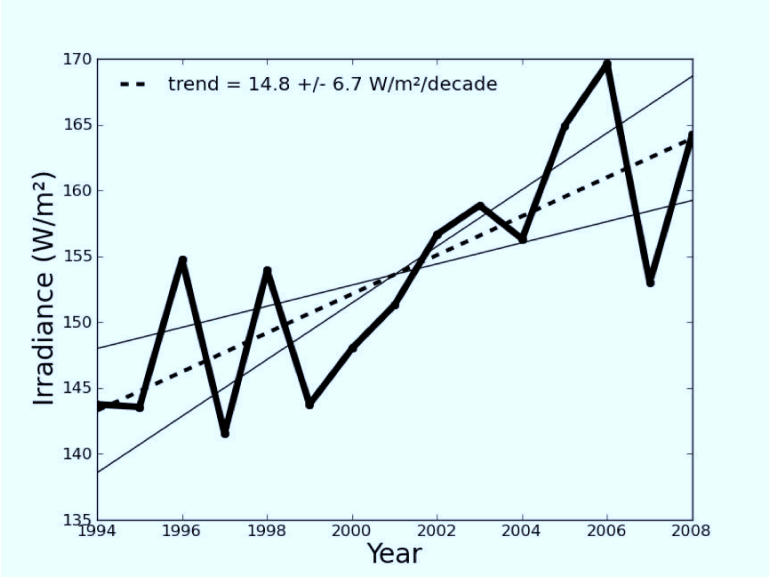

Figure 5.12: Winter average reconstructed downwelling radiation for Resolute. The linear fit of the downwelling irradiance has a slope of 14.8 $\pm$ 6.7 $Wm^{-2}decade^{-1}$. (repeat of Figure 2.11)

The large uncertainty in the clear sky irradiance comes from the temperature's effect on it, as shown in Figure 5.14(a). The very large relative uncertainty in the temperature-driven irradiance swamps the signal from the water vapour effect, which is significantly increasing over the time period and displayed in Figure 5.14(b). Once again, closure of the two effects is maintained and this is shown in Figure 5.15 where the total change in downwelling irradiance and the sum of the change due to water vapour and temperature are compared.

With the total downwelling irradiance strongly increasing but the clear sky irradiance showing uncertainty as to whether or not it is truly trending upwards, it will not be surprising that the cloudy sky irradiance for Resolute was very strongly increasing (Figure 5.16).

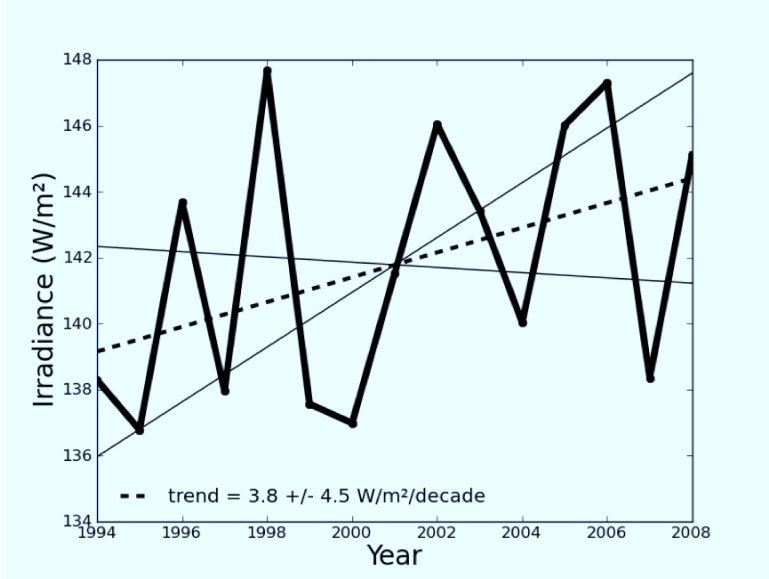

Figure 5.13: Winter average reconstructed clear sky downwelling radiation for Resolute. The linear fit of the downwelling irradiance has a slope of 3.8 ± 4.5 Wm^{-2}decade^{-1}. The clear sky irradiance is calculated by re-running the SBDART code with clouds removed.

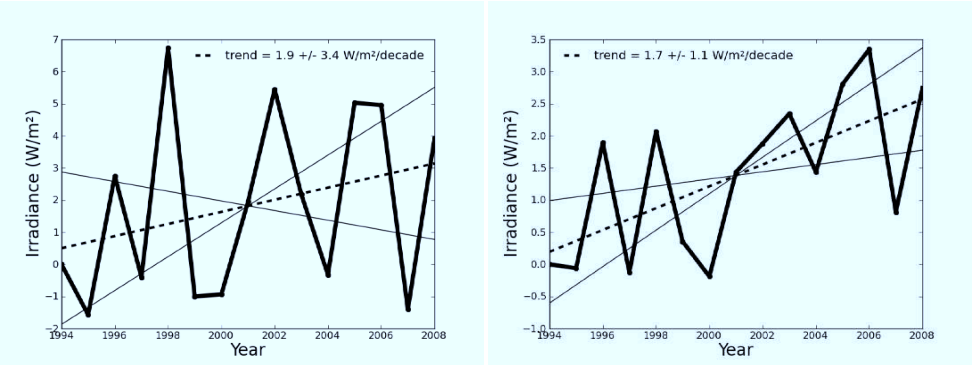

(a) Temperature effect

(b) Water vapour effect

Figure 5.14: (a) Temperature's effect on irradiance for Resolute. The linear fit of the temperature effect has a slope of 1.9 ± 3.4 Wm^{-2}decade^{-1}. This is the change in irradiance since the starting winter due to changing temperature. To calculate this value, the SBDART code was run with a constant water vapour profile (the all-radiosonde winter mean) while allowing the temperature to vary. (b) WV's effect on irradiance for Eureka Water vapour's effect on irradiance for Resolute. The linear fit of the water vapour effect has a slope of 1.7 ± 1.1 Wm^{-2}decade^{-1}. This is the change in irradiance since the starting winter due to changing water vapour. To calculate this value, the SBDART code was run with a constant temperature profile (the all-radiosonde winter mean) while allowing the water vapour to vary.

Table 5.2: Summary of irradiance contributions at Resolute

Effect	Contribution per decade
Cloud	11.0 Wm^{-2}
Clear (Water vapour/Temperature)	3.8 (1.7/1.9) Wm^{-2}
Total	14.8 Wm^{-2}

This increase is much larger than that at Eureka, and is due to increasing average relative humidity, shown in Figure 5.17(a) (and 5.17(b) respectively).

To further support the increasing cloud-included irradiance, the surface observed cloud fraction is significantly increasing over the time period, at about 1 tenth per decade. This increase is shown in Figure 5.18. Note that in the case of Eureka, there was no significant trend in this parameter, while at Resolute the trend is significant.

Table 5.2 summarizes the contributions to increasing irradiance at Resolute.

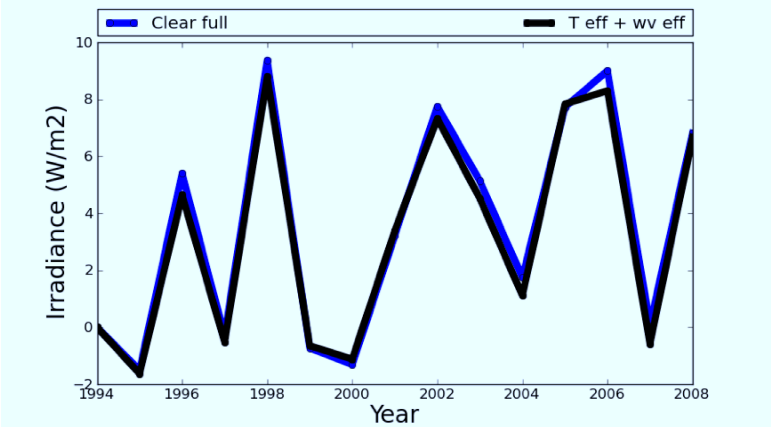

Figure 5.15: Closure of the effects of water vapour and temperature on irradiance for Resolute. The blue line is the change in irradiance since 1994 in the full clear sky simulation (water vapour and temperature varying), and the black line is the sum of the water vapour and temperature effects shown in Figures 5.14(b) and 5.14(a) respectively.

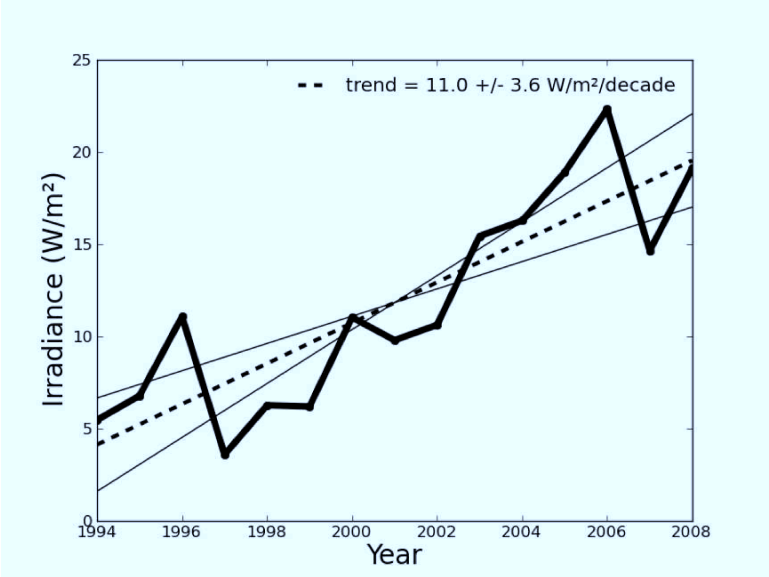

Figure 5.16: Winter averaged reconstruction of the effect of clouds on irradiance at Resolute. The linear fit of the cloud effect has a slope of 11.0 ± 3.6 Wm^{-2}decade^{-1}. The cloud effect is calculated by subtracting the clear sky irradiance from the full simulated irradiance.

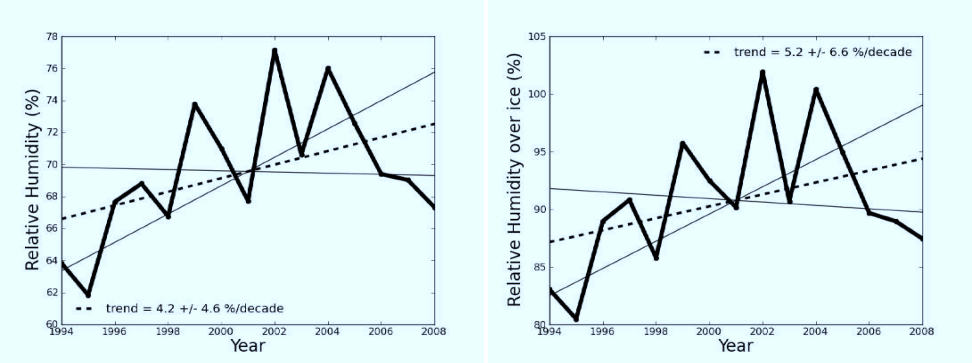

(a) RH (b) RHice

Figure 5.17: Lower-troposphere relative humidity with respect to water (a) and with respect to ice (b) time-series at Resolute. Values are averages over the whole winter, and the linear fit has a slope of 4.2 ± 4.6 % decade^{-1} in (a) and 5.2 ± 6.6 % decade^{-1} in (b). The lower-troposphere relative humidity is an average of the relative humidity from the surface to 5 km.

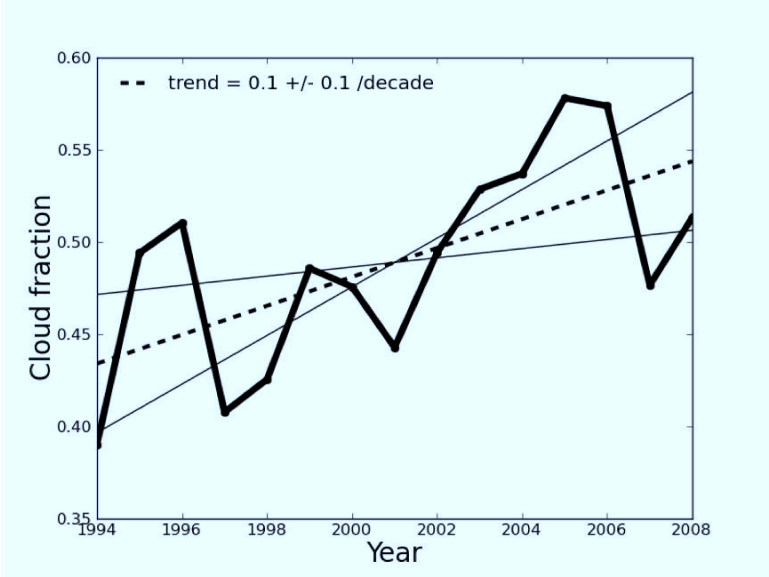

Figure 5.18: Surface observed cloud fraction time-series at Resolute. Values are averages over the whole winter, and the linear fit has a slope of 0.1 ± 0.1 decade^{-1}.

5.2 Surface Fluxes

5.2.1 Eureka

Accompanying the increasing downwelling radiation at Eureka is a similar, if weaker, increase in the upwelling irradiance, shown in Figure 5.19(a). This increase is no doubt a response to the forcing from the atmosphere that must be balanced in the surface energy budget. Any increase in net surface-ward energy is going to elicit a response from the skin temperature, which must increase to bring the total net energy flux back to zero, because the upwelling radiation is a direct function of skin temperature and is also the only flux which corresponds to an assured energy loss for the surface skin over the winter. Figure 5.19(b) shows the skin temperature (and air temperature), and it is not surprising at all that the skin temperature and therefore the upwelling radiation show a significant increase in the wake of the increasing downwelling forcing.

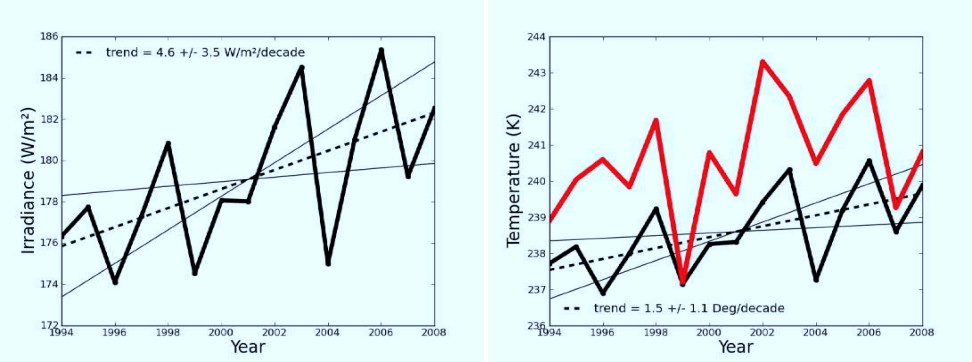

(a) Upwelling radiation (b) Skin temperature

Figure 5.19: (a) Winter average reconstructed upwelling radiation at Eureka. The linear fit has a slope of 4.6 $\pm$ 3.5 Wm^{-2} decade^{-1}. (b) Winter average reconstructed skin temperature (black) and measured surface air temperature (red) at Eureka. The linear fit of skin temperatures has a slope of 1.5 $\pm$ 1.1 K decade^{-1}, compared to the slope of 1.3 K decade^{-1} for the air temperature.

The increasing skin temperature, which follows the upward trend of the air temperature, dampens the potential for increased sensible cooling through diffusion by the warmer atmosphere. Since the air is very stable directly above the surface, the diffusive sensible heat flux will be an important factor in the cooling of the atmosphere above the surface. If the skin temperature were to remain constant for whatever reason in the presence of the

warming air, a negative feedback would be present for the air temperature, where the increased air-surface gradient would in fact increase the rate of cooling of the atmosphere due to the mixing transport of thermal energy. This is, however, not the case, as evidenced by Figure 5.21 which shows if anything a decrease in the turbulent fluxes.

With the skin temperature increasing, the temperature gradient between the surface and the ground below it will decrease provided that the sub-surface temperatures are not also increasing. Figure 5.22(b) shows that the increase in temperature at 1 m depth is statistically unlikely in comparison to the skin temperature increase, which should lead to a weakening of the surface-ward conductive flux. Figure 5.22(a) shows that this is possibly the case, although the large uncertainty clouds this conclusion. The uncertainty in the conductive flux trend is related to the large uncertainty in the sub-surface temperature, but is also exacerbated by the year-to-year variations of snow cover which greatly affect this quantity. Over this time period, the average winter snow depth fluctuates between 5 cm and 25 cm, with jumps of up to 12 cm between years. Given the strong insulating effect that snow has on the conduction from below, the surface to soil temperature gradient must share its role as driver of the conductive flux.

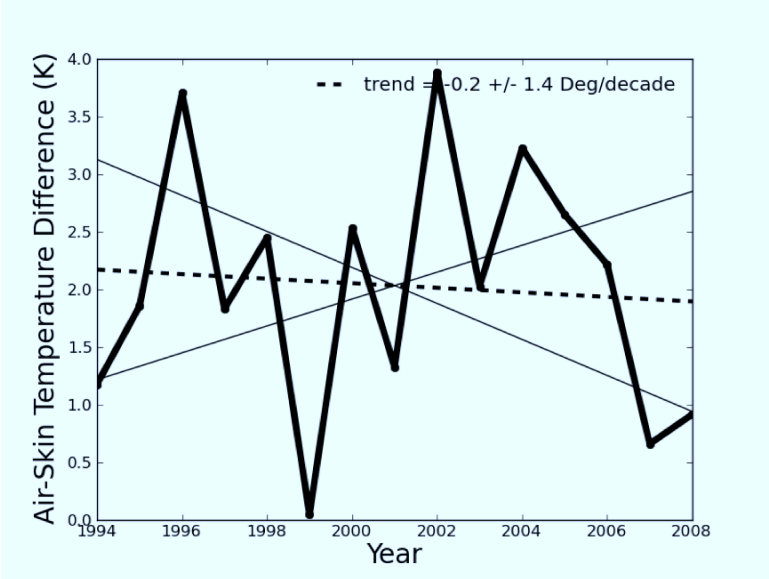

Figure 5.20: Winter average skin-air temperature difference at Eureka. The linear fit has a slope of -0.2 $\pm$ 1.4 K decade^{-1}.

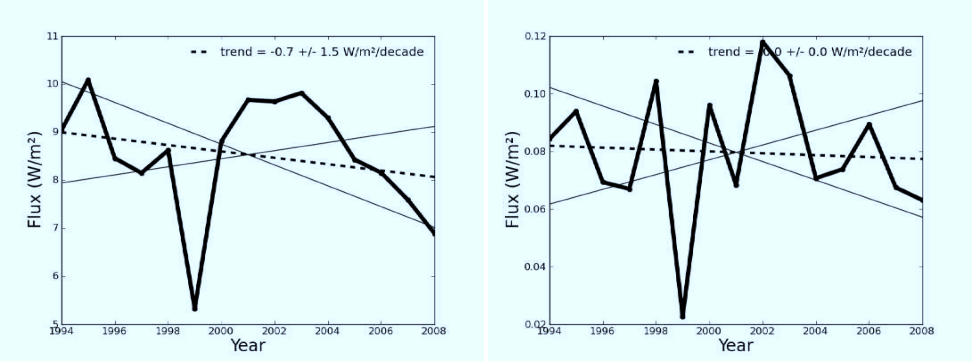

(a) Sensible heat (b) Latent heat

Figure 5.21: (a) Winter average reconstructed sensible heat flux at Eureka. The linear fit has a slope of -0.7 $\pm$ 1.5 Wm^{-2} decade^{-1}. The large dip in the winter 1999 is likely mostly due to an anomalous minimum in average wind speed during that year (not shown), and overall the wind speed shows no trend over the winters of this time period. (b) Winter average reconstructed latent heat flux at Eureka. The linear fit has a slope of 0.0 $\pm$ 0.01 Wm^{-2} decade^{-1}.

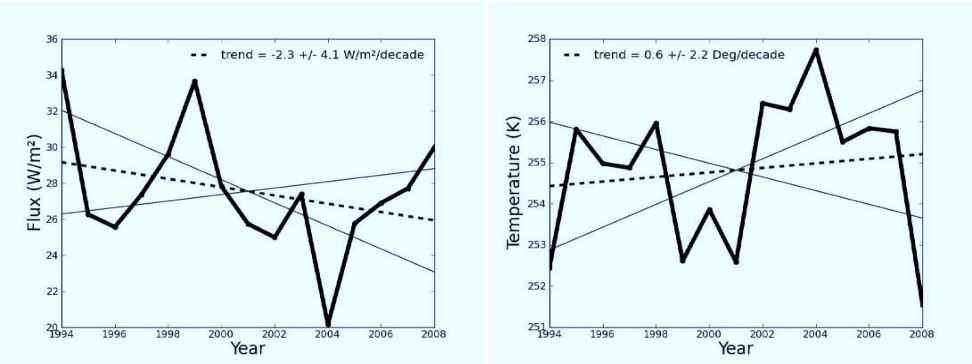

(a) Conductive flux (b) 1 m temperature

Figure 5.22: (a) Winter average reconstructed conductive flux at Eureka. The linear fit has a slope of -2.3 $\pm$ 4.1 Wm^{-2} $decade^{-1}$. (b) Winter average reconstructed temperature at 1 m depth at Eureka. The linear fit has a slope of 0.6 $\pm$ 2.2 K $decade^{-1}$.

5.2.2 *Resolute*

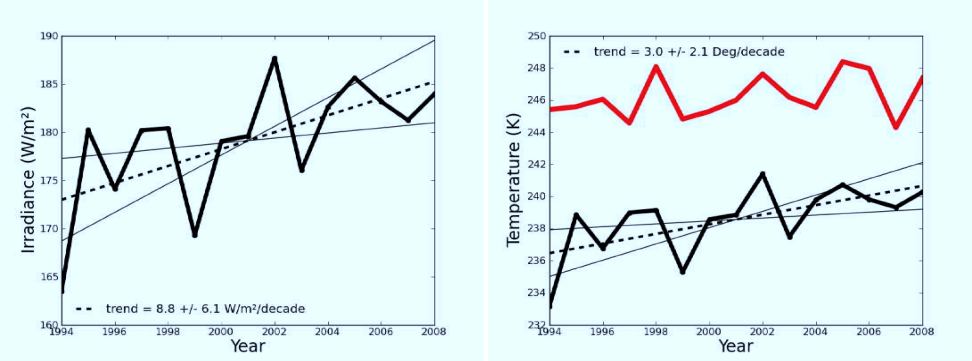

(a) Upwelling radiation (b) Skin temperature

Figure 5.23: (a) Winter average reconstructed upwelling radiation at Resolute. The linear fit has a slope of 8.8 ± 6.1 Wm^{-2} decade^{-1}. (b) Winter average reconstructed skin temperature (black) and measured surface air temperature (red) at Resolute. The linear fit of skin temperatures has a slope of 3.0 ± 2.1 K decade^{-1}.

At Resolute, the effect of increased downward irradiance on the skin temperature and upwelling radiation is similar to that at Eureka, and in fact stronger. The skin temperature, and the upwelling radiation it is responsible for, show significant increases over the decade and a half of interest in Figures 5.23(b) and 5.23(a) respectively. Of particular note in this study is the substantially larger air-surface temperature difference at Resolute than at Eureka. This difference is due to greater snow cover at Resolute (see Figure 3.2(a)) which isolates the surface from conductive flux responses to a highly radiatively cooling surface. This is verified by replacing Resolute's snow cover with Eureka's for a simulation run, which results in a magnitude for the Resolute air-skin temperature difference very similar to that of Eureka. This is also reflected in the first year of the time period plotted, where the average air-skin temperature difference was 12 degrees. Not coincidentally, this happens to be the winter with the second-largest snow depth on record (since 1953), with an average snow depth of over 42 cm, which is more than double that of almost all the other years of this study. Figure 5.24 shows the correlation between average winter snow cover and average winter conductive flux for Resolute (a) and Eureka (b).

Again similarly to Eureka, the turbulent fluxes at Resolute are either decreasing or likely not trending significantly, as shown in Figure 5.25(a) and 5.25(b). The magnitude of each is larger than at Eureka, which would result from the increased surface-atmosphere

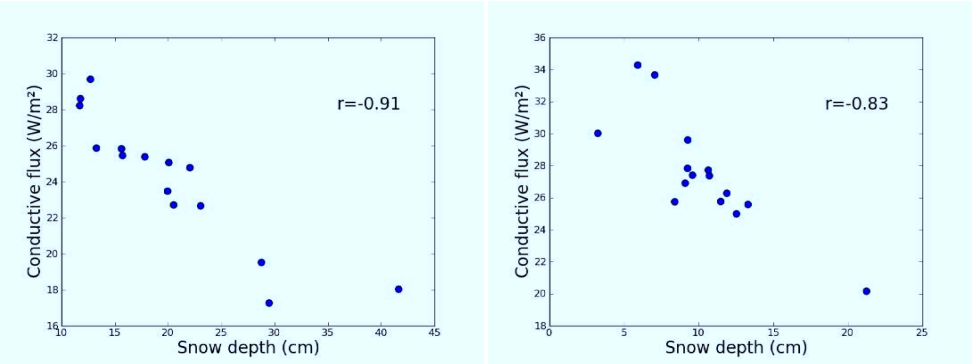

(a) Resolute (b) Eureka

Figure 5.24: (a) Correlation of average winter surface conductive flux with average winter snow depth for Resolute. There is a strong negative correlation, meaning that years when the surface was more insulated from the soil, it was allowed to cool more. (b) Correlation of average winter surface conductive flux with average winter snow depth for Eureka. There is a strong negative correlation, as there is at Resolute.

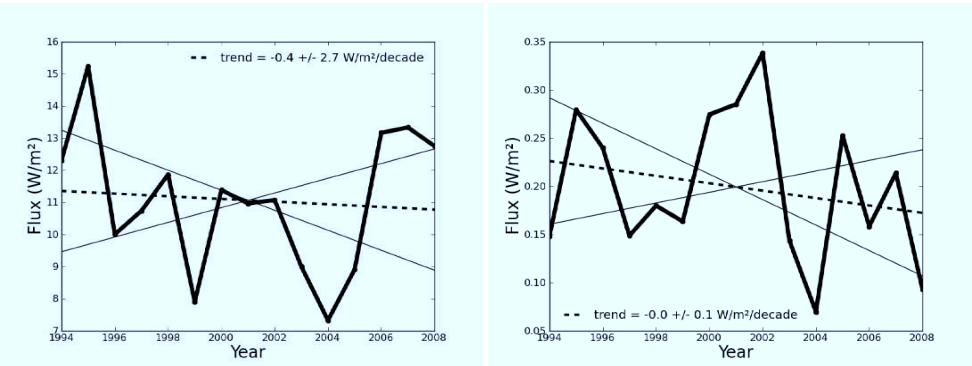

(a) Sensible heat (b) Latent heat

Figure 5.25: (a) Winter average reconstructed sensible heat flux at Resolute. The linear fit has a slope of -0.4 $\pm$ 2.7 Wm^{-2} $decade^{-1}$. (b) Winter average reconstructed latent heat flux at Resolute. The linear fit has a slope of -0.03 $\pm$ 0.1 Wm^{-2} $decade^{-1}$.

temperature difference. Unlike at Eureka, this temperature difference has been decreasing over the studied time period, and significantly so.

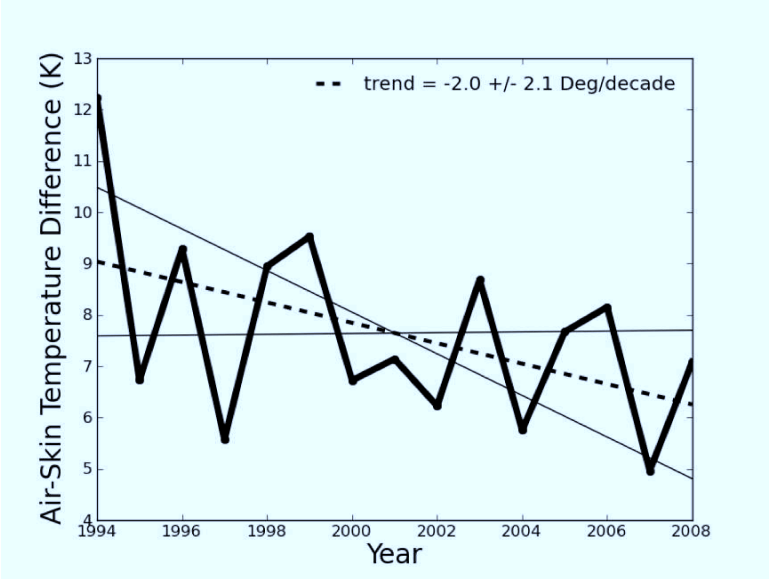

Figure 5.26: Winter average skin-air temperature difference at Resolute. The linear fit has a slope of -2.0 $\pm$ 2.1 K decade^{-1}.

At Eureka, this difference was held steady by the reduced conduction from below, which allowed the upwelling radiation to not have to shoulder the entire load of keeping the surface skin in energy balance. At Resolute, however, there is no measured downward trend in the conductive flux (Figure 5.27(a)). This forces almost all of the balancing of the increased downwelling radiation to come from the upwelling radiation (and thus the temperature of the skin).

5.3 Surface Balance Summary and Discussion

Figure 5.28 shows the trajectory of the surface energy balance for both Eureka and Resolute in state space. Each point corresponds to the winter average for a given year of net radiation along the x-axis and conductive flux along the y-axis. Since the sum of these two and the sensible heat (plus latent heat) must equal zero, the dashed lines are of constant sensible plus latent heat flux and decrease from the bottom left to upper right of the figure. Eureka's trajectory shows a greater range of variation of both conductive flux and net radiation, moving for the most part along lines of constant sensible heat. Resolute, on the other hand,

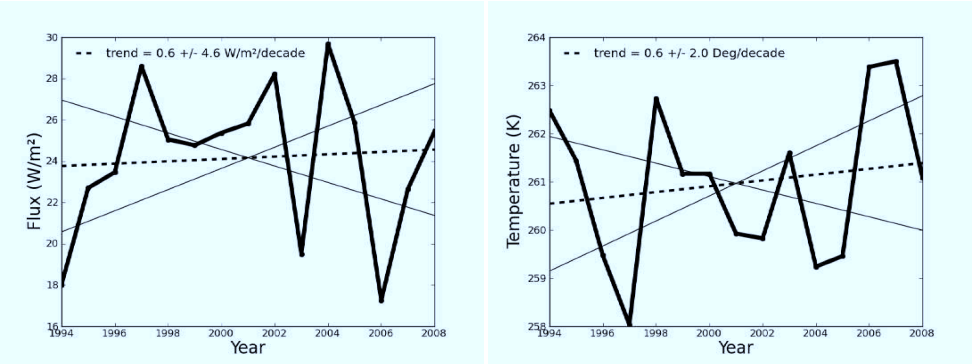

(a) Conductive flux (b) 1 m temperature

Figure 5.27: (a) Winter average reconstructed conductive flux at Resolute. The linear fit has a slope of 0.6 ± 4.6 Wm^{-2} decade^{-1}. (b) Winter average reconstructed temperature at 1 m depth at Resolute. The linear fit has a slope of 0.6 ± 2.0 K decade^{-1}.

shows less range in both the x- and y-directions and more variability in sensible heat.

One of the stated goals of this work is to gain understanding of the causes of the enhanced warming of the Arctic surface. In this study, the main suspects appear to be the enhanced downwelling radiation caused by temperature, by water vapour, and by clouds. This enhanced downwelling irradiance warms the surface, and the conductive flux partially adjusts to compensate, but not nearly enough to mitigate the significantly increasing energy input. Instead, the surface warms and compensates for the downward forcing by sending out more radiant energy.

Another kind of enhancement that is an important part of Arctic Amplification is that of the surface temperature trend compared to the trend of the troposphere as a whole. To illustrate this, Figure 5.29 shows the time series of average tropospheric temperature, calculated as the mean from the surface to the 400 hPa pressure level. The 400 hPa level is chosen to capture much of the troposphere, while being assured to avoid the stratosphere. A comparison to Figures 5.1, and 5.19(b) shows that the surface air and skin temperatures at Eureka are increasing more than the average temperature of the atmosphere aloft by a factor of 2-3.

To restate the problem of the discrepancy of warming with height, it is instructive to use the surface energy balance in the form

$$\epsilon_{sky}\sigma T_{sky}^4 - \epsilon_{snow}\sigma T_s^4 + SH + C = 0 \tag{5.1}$$

where ϵ_{sky} is the effective emissivity of the atmosphere and T_{sky} is the emission temperature of the atmosphere, so by definition the first term of equation 5.1 is the downwelling irradiance:

$$DW = \epsilon_{sky}\sigma T_{sky}^4. \tag{5.2}$$

Finitely differentiating equation 5.1 and assuming that non-linear terms of the result are small gives

$$4\epsilon_{sky}\sigma T_{sky}^3 \Delta T_{sky} - 4\epsilon_{snow}\sigma T_s^3 \Delta T_s + \Delta SH + \Delta C = 0 \tag{5.3}$$

which can be used to assess the sensitivity of the radiation terms to changes in sky and skin temperature. If Eureka's values from the reconstruction for T_s (238.5 K) and ΔT_s (1.5 K decade^{-1}) are used, the resulting change in upwelling radiation is 4.6 Wm^{-2}decade^{-1}, agreeing perfectly with the modeled change in upwelling irradiance (see Figure 5.19(a)). Using ΔSH + ΔC from the reconstruction as well, the reconstructed ΔDW of 7.6 Wm^{-2}decade^{-1} is obtained. The problem arises when the required change in sky temperature to account for this change in downwelling irradiance is calculated. By using the average tropospheric temperature from Figure 5.29(a), and a sky emissivity of 1, a minimum estimate for the required change in sky temperature is calculated to be 2.3 K decade^{-1}, which is much larger than the observed tropospheric temperature change of 0.6 K decade^{-1}, and outside the interval of 95 percent confidence for the tropospheric temperature trend.

With the only inconsistency from equation 5.3 coming from the combined use of the downwelling irradiance term and the average tropospheric temperature, two options for reconciliation present themselves. The first is to find another temperature which better represents the relationship of equation 5.2, and the other is to find a better relationship that applies to the average tropospheric temperature. For the current work, the latter is chosen, as the Stefan-Boltzmann relation (equation 5.2) is meant to apply to a broadband blackbody emitter, which the atmosphere is not.

To find the relationship between T_{sky} and DW, a power law fit is performed on the collection of tropospheric temperatures and downwelling irradiances from all winter soundings for the time period 1994-2009. The results of the fit for Eureka and Resolute are plotted in Figure 5.30.

The resulting empirical equation for the downwelling irradiance in terms of average atmospheric temperature becomes

$$DW = aT_{sky}^{n} \tag{5.4}$$

where the fit parameters are calculated to be a = 1.16 x$10^{-15\pm1}$ and n = 7.2$\pm$1.0 for Eureka. The greater-than-fourth power of temperature in the fit implies that the effective emissivity of the sky has a dependence on temperature. This is likely due to the correlation between the water vapour content (as well as clouds) and the temperature of the air that is advected to Eureka. The fact that the downwelling irradiance is proportional to a power greater than four of the tropospheric temperature makes it likely that small changes in atmospheric temperature have a greater effect on the downward irradiance than similar changes in skin temperature have on the upwelling irradiance. The sensitivity of the downwelling irradiance according to equation 5.4, at 243 K, is 3.1 $\mathrm{Wm^{-2}K^{-1}}$, but with a very large uncertainty. Such a precise calculation of the sensitivity of the downwelling irradiance to a temperature change is not meaningful, however, as the uncertainty in fit parameter a spans more than an order of magnitude.

The fit result does, however, agree with the work of Swinbank (1963), who showed that the downwelling long-wave flux should equal 5.31x$10^{-13}T_{air}^{6}$ for clear skies, because the effective emissivity is proportional to the air temperature squared on the climatological scale. The fit also agrees with the regression by *King* (1996), who found that the downwelling irradiance from the stable atmosphere above Antarctic stations had the relationship 1.31x$10^{-13}T_{M}^{6.29}$ with the temperature at the top of the surface inversion T_M.

From this relationship between downwelling irradiance and temperature, the criteria for surface enhancement of warming can be deduced. If constant conductive and sensible heat fluxes are assumed, for simplicity, the sixth power relationship of atmospheric temperature opens the door for increased temperature sensitivity of the surface compared to the atmosphere, since the surface must make up any increase in downwelling irradiance by its own increase in upwelling irradiance. With the assumption of ΔSH, ΔC = 0, and the approximate empirical power law for the downwelling irradiance, equation 5.3 takes the form

$$naT_{sky}^{n-1}\Delta T_{sky} - 4\epsilon\sigma T_{s}^{3}\Delta T_{s} = 0 \tag{5.5}$$

from which the expression for surface enhancement follows:

$$\frac{\Delta T_s}{\Delta T_{sky}} = \frac{n}{4}\frac{a}{\epsilon\sigma}\frac{T_{sky}^{n-1}}{T_s^3} \tag{5.6}$$

where $\frac{\Delta T_s}{\Delta T_{sky}}$ is the surface amplification factor A_s, as a sensitivity of skin temperature to change in tropospheric temperature. The criterion for surface enhancement of warming is then $A_s > 1$, or

$$\frac{T_{sky}^{n-1}}{T_s^3} > \frac{4}{n}\frac{\epsilon\sigma}{a} \tag{5.7}$$

where the right-hand side this equation is equal to $\sim$2.73x10^7. The temperatures of troposphere and skin since 1994 are such that this criterion is met, with an average surface amplification factor of 1.34. While this factor is smaller than the observed enhancement of 2.5 in comparing change in tropospheric temperature to change in skin temperature over that period, the uncertainties involved in all fit parameters and temperature changes are high.

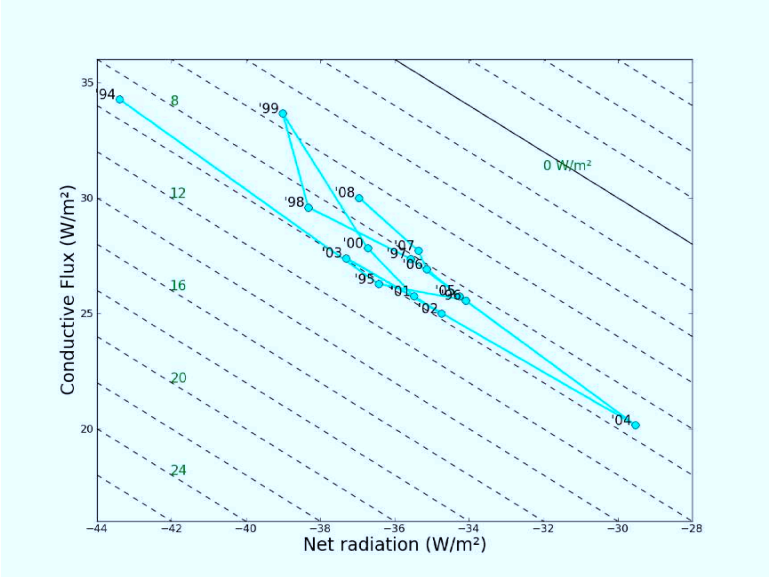

(a) Eureka

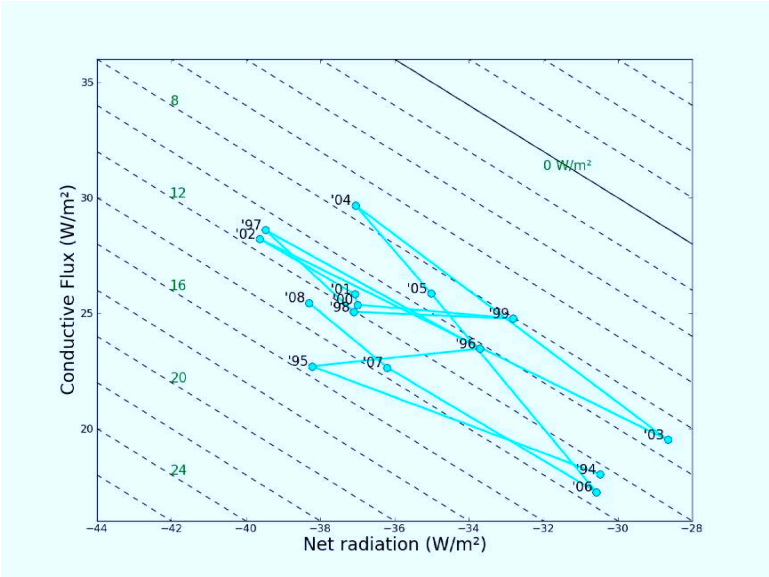

(b) Resolute

Figure 5.28: Trajectory in surface energy balance state-space for Eureka (a) and Resolute (b). The x- and y-axis present net radiation and conductive flux, respectively, while the diagonal dashed lines are of constant sensible plus latent heat.

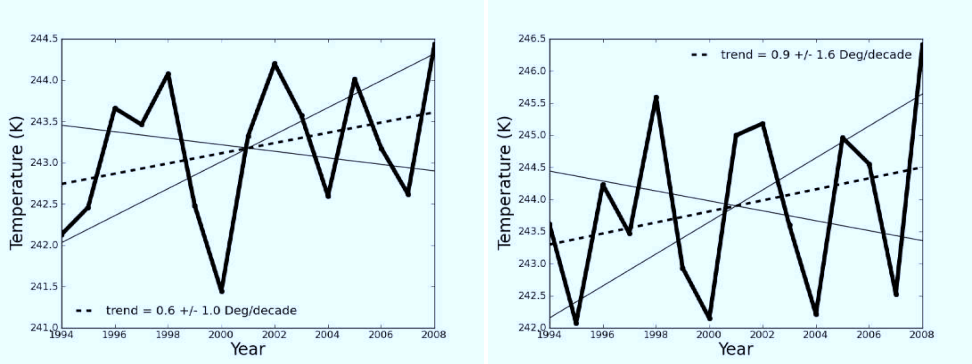

(a) Eureka (b) Resolute

Figure 5.29: Winter average mean tropospheric temperature for Eureka (a) and Resolute (b). The linear fit has a slope of 0.6 ± 1.0 K decade^{-1} for Eureka and 0.9 ± 1.6 K decade^{-1} for Resolute.

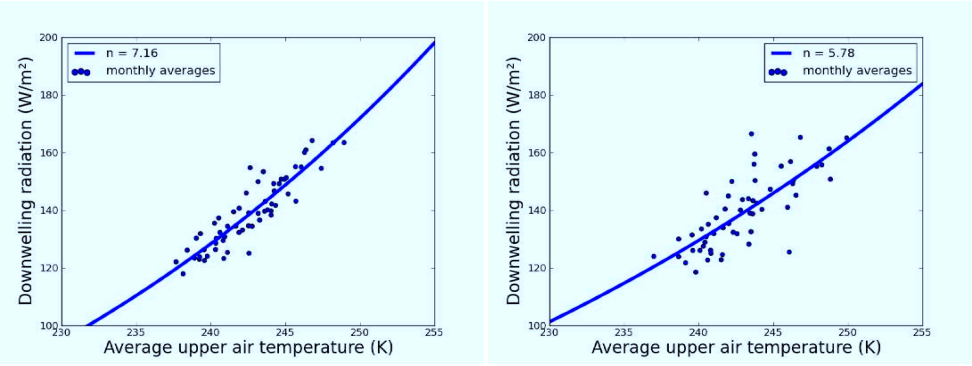

(a) Eureka (b) Resolute

Figure 5.30: Power law fits of downwelling irradiance as a function of average tropospheric temperature for Eureka (a) and Resolute (b). The fit was to the equation $DW = aT_{sky}^{n}$. The fit parameters are found to be n = 7.16 and a = 1.16 x10^{-15} for Eureka and n = 5.78 and a = 2.3 x10^{-12} for Resolute.

CHAPTER 6

CONCLUSION

The surface energy balance in the Arctic winter is mainly driven by atmospheric long-wave irradiance. A method of modeling this downwelling irradiance in all sky conditions during the dark season in the High Arctic is presented and used to retrodict the behaviour of downwelling irradiance since 1994. This reconstruction of downwelling long-wave irradiance requires a method for deducing cloud locations from radiosonde profiles, which is introduced and shown to give less than 10% average error in a clouded-sky comparison with lidar-derived downwelling irradiance. Using this radiosonde cloud method and the SBDART radiative transfer code, the reconstruction of downwelling long-wave irradiance shows an increasing trend of 7.9 Wm^{-2} per decade at Eureka and 14.8 Wm^{-2} per decade at Resolute over the time period of the winters 1994-2009. The radiative transfer model is used to decompose this increase into component effects of water vapour, temperature and clouds. The water vapour and temperature components of the changing irradiance show increasing trends of 1.7 Wm^{-2} and 1.9 Wm^{-2} per decade at Resolute, and 1.7 Wm^{-2} and 2.1 Wm^{-2} per decade at Eureka. The majority of the increase in total downwelling irradiance is shown to be from the contribution of clouds, which has a trend of 4.4 Wm^{-2} per decade at Eureka and 11.0 Wm^{-2} per decade at Resolute.

Because the region below the surface also has an important effect on the surface energy balance, a method of modeling sub-surface winter temperatures at Resolute and Eureka is presented and used to reconstruct historical temperature profiles. This method is compared to soil temperature measurements taken at Resolute and shown to reasonably reproduce winter-to-winter variations as well as changes within a given winter. This sub-surface

model coupled to the surface energy balance, with inputs from the above downwelling irradiance and sensible and latent heat fluxes based on radiosondes, is used to reconstruct the winter surface energy budget from 1994 to 2009. This collection of the important surface fluxes shows no significant trends in the conductive flux, latent heat, and sensible heat, while showing significant increase in the upwelling irradiance and skin temperature in response to the previously presented increase in downwelling irradiance. The snow cover is shown to be the primary indicator of surface conductive flux at both Eureka and Resolute, with very strong anti-correlations (-0.83 and -0.91 respectively) between snow depth and conductive flux to the surface.

An exponential fit is performed to find that the power-law relationship between downwelling irradiance and average tropospheric temperature has a power greater than 4 (7.18 for Eureka and 5.78 for Resolute). This departure from the Stefan-Boltzmann law is an indication that the effective emissivity of the atmosphere is strongly correlated with atmospheric temperature in the Arctic, and creates the possibility that the surface temperature has a high sensitivity to changes in atmospheric temperature. The resulting enhancement factor for surface temperature changes in comparison to atmospheric temperature changes for Eureka is found theoretically to be 1.34, which does not account for the entire difference in observed atmospheric and surface temperatures (observed factor of 2.5 enhancement). This indicates that future work is required to find the remaining factors in the surface enhancement of temperature change, which could be strongly dependent on local effects such as down-slope flow from nearby ridges.

The increase in downwelling irradiance has important implications for the surface in the High Arctic. As downwelling radiation is the main source of energy to the surface in the Arctic winter, large increases in this flux of energy will have an important warming effect. The fact that the warming is greatly affected by an increase in water vapour, which both directly causes increased irradiance and also causes higher relative humidities and thus more cloud irradiance, is an indication of the proposed water vapour climate feedback: reduced sea-ice increases atmospheric water vapour, which warms the surface through radiation and further reduces sea-ice due to the warmer temperatures.

The strong dependence on snow cover of conductive flux makes future snowfall rates in the High Arctic an important part of the changing climate. If more clouds also leads to more precipitation, the increased downwelling irradiance due to these clouds would be

somewhat offset by the reduced conductive flux that accompanies increased snow cover. To properly diagnose the conductive fluxes, it is strongly recommended that soil temperature measurements like those that took place at Resolute are restarted and sustained for as long as possible. The temperature information gathered by these sensors is invaluable for deducing the effect of the changing climate on soil and permafrost. Along with soil temperature measurements, a co-located suite of atmospheric flux instruments would allow measurements of the total surface energy budget. The sustained measurement of sensible and latent heat fluxes from the atmosphere to the surface, similar to the one-year study SHEBA, would grant insight about their role in Arctic climate change and Arctic Amplification.

BIBLIOGRAPHY

Aggarwal, R., P. Negi, and P. Satyawali, New density-based thermal conductivity equation for snow, *Defence Science Journal*, *59*, 126–130, 2009.

Alexeev, V., P. Langen, and J. Bates, Polar amplification of surface warming on an aquaplanet in ghost forcing experiments without sea ice feedbacks., *Clim. Dyn.*, *24*, 655–666, 2005.

Arabey, E., Radiosonde data as means for revealing cloud layers, *Meteor. Gidrol.*, *6*, 32–37, 1975.

Bradley, R., and F. Keimig, Climatology of surface-based inversions in the north american arctic?, *Journal Of Geophysical Research*, *97*, 15,699–15,712, 1992.

Brown, R., P. Bartlett, M. MacKay, and D. Verseghy, Evaluation of snow cover in class for snowmip, *Atmosphere-Ocean*, *44*, 223–238, 2006.

Chernykh, I., and R. Eskridge, Determination of cloud amount and level from radiosonde soundings, *Journal of Applied Meteorology*, *35*, 1362–1369, 1996.

Chylek, P., C. Foland, G. Lesins, and M. Dubey, Arctic air temperature change amplification and the atlantic multidecadal oscillation, *Geophys. Res. Lett.*, *36*, L14,801, 2009.

Curry, J., W. Rossow, D. Randall, and J. Schramm, Overview of arctic cloud and radiation characteristics, *Journal of Climate*, *9*, 1731–1764, 1996.

Doyle, J., G. Lesins, C. Thackray, C. Perro, G. Nott, T. Duck, R. Damoah, and J. Drummond, Water vapor intrusions into the high arctic during winter, *Geophysical research letters*, *9*, 1731–1764, 2011.

Foken, T., The energy balance closure problem: An overview, *Ecological Applications*, *18*, 1351–1367, 2008.

Francis, J., and E. Hunter, Changes in the fabric of the arctic's greenhouse blanket, *Environmental Research Letters*, *2*, 045,011, 2007.

Fukusako, S., Thermophysical properties of ice, snow, and sea ice, *International Journal of Thermophysics*, *11*, 353–372, 1990.

Grachev, A., E. Andreas, C. Fairall, P. Guest, and P. G. Persson, Sheba fluxprofile relationships in the stable atmospheric boundary layer, *Boundary-Layer Meteorol*, *124*, 315–333, 2007.

Graversen, R., Do changes in the midlatitude circulation have any impact on the arctic surface air temperature trend?, *J. Clim.*, *19*, 5422–5438, 2006.

Hansen, J., M. Sato, R. Ruedy, and L. Nazarenko, Efficacy of climate forcing, *J. Geophys. Res.*, *110*, –, 2005.

Hindmarsh, A., Lsode and lsodi, two new initial value ordinary differnetial equation solvers, *ACM SIGNUM Newsletter*, *15*, 10–11, 1980.

Holland, M., and C. Bitz, Polar amplification of climate change in coupled models, *Climate Dynamics*, *21*, 221–232, 2003.

Jin, X., J. Hanesiak, and D. Barber, Detecting cloud vertical structures from radiosondes and modis over arctic first-year sea ice, *Atmospheric Research*, *83*, 64–76, 2007.

Jordan, R., E. Andreas, and A. Makshtas, Heat budget of snowcovered sea ice at north pole, *J. Geophys. Res.*, *104*, 7785–7806, 1999.

Jorgenson, M., V. Romanovsky, J. Harden, Y. Shur, J. O'Donnell, A. Schuur, M. Kanevsky, and S. Marchenko, Resilience and vulnerability of permafrost to climate change, *Canadian Journal of Research*, *40*, 1219–1236, 2010.

King, J., Longwave atmospheric radiation over antarctica, *Antarctic Science*, *8*, 105–109, 1996.

Kondo, J., and H. Yamazawa, Measurements of snow surface emissivity, *Boundary-Layer Meteorology*, *34*, 415–416, 1985.

Lesins, G., T. Duck, and J. Drummond, Climate trends at eureka in the canadian high arctic, *Atmosphere-Ocean*, *0*, 0, 2010.

Ling, F., and T. Zhang, A numerical model for surface energy balance and thermal regime of the active layer and permafrost containing unfrozen water, *Cold Regions Science and Technology*, *38*, 1–15, 2004.

Manabe, S., and R. Stouffer, Sensitivity of a global climate model to an increase of co2 concentration in the atmosphere, *Journal Of Geophysical Research*, *85*, 5529–5554, 1980.

Marty, C., et al., Downward longwave irradiance uncertainty under arctic atmospheres: Measurements and modeling, *Journal Of Goephysical Research*, *108*, 2003.

Matsui, N., C. Long, D. Augustine, and D. Halliwell, Evaluation of arctic broadband surface radiation measurements, atmospheric measurement techniques, *Submitted*, *0*, –, 2011.

Miloshevich, L., H. Vomel, D. Whiteman, B. Lesht, and F. Russo, Absolute accuracy of water vapor measurements from six operational radiosonde types launched during awex-g and implications for airs validation, *Journal of Geophysical Research*, *111*, D09S10, 2006.

Monin, A., and A. Obukhov, Basic laws of turbulent mixing in the surface layer of the atmosphere., *Trudy Geofiz Inst Acad Nauk SSSR*, *24*, 163–187, 1954.

Moritz, R., C. Bitz, and E. Steig, Dynamics of recent climate change in the arctic, *Science*, *297*, 1497–1502, 2002.

Persson, P. G., C. Fairall, E. Andreas, P. Guest, and D. Perovich, Measurements near the atmospheric surface flux group tower at sheba: Near-surface conditions and surface energy budget, *J. Geophys. Res.*, *107*, SHE 21 1–35, 2002.

Prata, A., A new long-wave formula for estimating downward clear-sky radiation at the surface, *Q. J. R. Meteorol. Soc*, *122*, 1127–1151, 1996.

Ricchiazzi, P., S. Yang, C. Gautier, and D. Sowle, Sbdart: A research and teaching software tool for plane-parallel radiative transfer in the earths atmosphere, *Bulletin of the American Meteorological Society*, *79*, 2101–2114, 1998.

Screen, J., and I. Simmons, The central role of diminishing sea ice in recent arctic temperature amplification, *Nature*, *464*, 1334–1337, 2010.

Serreze, M., and J. Francis, The arctic amplification debate, *Climatic Change*, *76*, 241–264, 2006.

Serreze, M., A. Barrett, J. Stroeve, D. Kindig, and M. Holland, The emergence of surface-based arctic amplification, *The Cryosphere*, *3*, 11–19, 2009.

Stamnes, K., S. Tsay, W. Wiscombe, and K. Jayaweera, Numerically stable algorithm for discrete-ordinate-method radiative transfer in multiple scattering and emitting layered media., *Applied Optics*, *27*, 2502–2509, 1988.

Turner, D., B. Lesht, S. Clough, J. Liljegren, H. Revercomb, and D. Tobin, Dry bias and variability in vaisala rs80-h radiosondes: The arm experience, *Journal of Atmospheric and Oceanic Technology*, *20*, 117–132, 2003.

Wan, Z., and J. Dozier, A generalized split-window algorithm for retrieving land-surface temperature from space, *Geoscience and Remote Sensing, IEEE Transactions on*, *34*, 892–905, 1996.

Wang, J., and W. Rossow, Determination of cloud vertical structure from upper-air observations, *Journal of Applied Meteorology*, *34*, 2243–2258, 1995.

Wang, X., J. Key, and Y. Liu, A thermodynamic model for estimating sea and lake ice thickness with optical satellite data, *J. Geophys. Res.*, *115*, C12,035, 2010.

Weller, G., and T. Schwerdtfeger, Thermal properties and heat transfer processes of the snow of the central antarctic plateau, *Glacial Meteorology*, *1*, 284–298, 1970.